
UNCERTAINTY QUANTIFICATION OF GRAPH CONVOLUTION NEURAL NETWORK MODELS OF EVOLVING PROCESSES

A PREPRINT

Jeremiah Hauth
University of Michigan,
Ann Arbor MI

Cosmin Safta
Sandia National Laboratories,
Livermore CA

Xun Huan
University of Michigan,
Ann Arbor MI

Ravi G. Patel
Sandia National Laboratories,
Albuquerque NM

Reese E. Jones*
Sandia National Laboratories,
Livermore CA

ABSTRACT

The application of neural network models to scientific machine learning tasks has proliferated in recent years. In particular, neural network models have proved to be adept at modeling processes with spatial-temporal complexity. Nevertheless, these highly parameterized models have garnered skepticism in their ability to produce outputs with quantified error bounds over the regimes of interest. Hence there is a need to find uncertainty quantification methods that are suitable for neural networks. In this work we present comparisons of the parametric uncertainty quantification of neural networks modeling complex spatial-temporal processes with Hamiltonian Monte Carlo and Stein variational gradient descent and its projected variant. Specifically we apply these methods to graph convolutional neural network models of evolving systems modelled with recurrent neural network and neural ordinary differential equations architectures. We show that Stein variational inference is a viable alternative to Monte Carlo methods with some clear advantages for complex neural network models. For our exemplars, Stein variational inference gave similar uncertainty profiles through time compared to Hamiltonian Monte Carlo, albeit with generally more generous variance. Projected Stein variational gradient descent also produced similar uncertainty profiles to the non-projected counterpart, but large reductions in the active weight space were confounded by the stability of the neural network predictions and the convoluted likelihood landscape.

1 Introduction

Scientific machine learning (SciML) [1] seeks to combine principles of machine learning (ML) with scientific computing to tackle complex problems that are often multiscale and multiphysical, exposed to uncertainty and noise, and where decisions carry high consequences. Neural networks (NNs) have emerged as a powerful tool in SciML due to their ability to learn and express complex nonlinear interactions. NNs have been applied to a wide range of tasks in this context, such as in subgrid surrogate modeling [2, 3, 4, 5], partial differential equations (PDEs) [6, 7, 8], and reinforcement learning [9, 10, 11]. These NNs easily reach hundreds, and even millions of parameters [12, 13, 14]. While expressive, a highly parameterized NN also becomes prone to over-fitting and poor generalizability if not treated carefully. Combined with the general lack of interpretability of NNs and the high-stakes nature of many SciML applications, a strong motivation emerges for uncertainty quantification (UQ) in NN models that is imperative for promoting transparency of model limitations and strengthening the trust of their predictions.

We focus on Bayesian UQ [15, 16, 17] that seeks to capture the uncertainty residing in model parameters. This entails performing Bayesian inference on the NN parameters. The resulting probabilistic NN, a NN where each parameter has a distribution of values instead of a single value, is also known as a *Bayesian neural network* (BNN) [18, 19, 20, 21, 22]. The Bayesian paradigm presents a principled framework to update parameter uncertainty, from a *prior* distribution to

*corresponding: rjones@sandia.gov

a *posterior* distribution, when new data becomes available. The central task for a Bayesian problem is thus to compute the posterior parameter distribution.

A conventional approach to Bayesian inference is to draw samples from the posterior distribution using Markov chain Monte Carlo (MCMC) algorithms [23, 24]. While MCMC methods offer desirable asymptotic convergence to the true posterior, they tend to converge slowly and do not scale well to high dimensional parameter spaces. While advanced MCMC variants such as Hamiltonian Monte Carlo (HMC) [25, 19] have been exercised for BNNs, the networks studied typically have had a few hundred parameters (e.g., [26, 27, 28]).

Variational inference (VI) [29, 30] is an alternative to MCMC that is more scalable. Instead of MCMC sampling, VI looks for a best approximate posterior from a family of tractable distributions, thereby turning a sampling task into an optimization problem. The simplest is perhaps mean-field VI [20, 21] that searches within the space of all *independent* Gaussian distributions. While very scalable to high dimensions, mean-field VI is unable to capture correlation among parameters and tends to underpredict the variance [29]. Beyond mean-field, particle-based Stein VI methods such as the Stein variational gradient descent (SVGD) [31] algorithm has demonstrated an attractive balance between computational scalability and an ability to capture general non-Gaussian distributions. However, SVGD has been observed to carry a tendency to collapse to the posterior mode when the particle-to-dimension ratio becomes low [32, 33]. More recently, the projected SVGD (pSVGD) [34] that forms a lower-dimensional posterior most informed by the data is able to increase the particle efficiency and mitigate the mode-collapse phenomenon. Both SVGD and pSVGD have only been lightly explored for usage in constructing BNNs [35, 36]; we will provide further study of the application of these algorithms in this paper.

We demonstrate SVGD and pSVGD on NNs of spatially complex, history dependent processes that emerge from SciML applications that are of interest in engineering and materials science. The first is homogenization of the inelastic mechanical response of stochastic volume elements of polycrystalline metals [2, 3]. The second models the process of out-gassing of a solid-state fuel [37, 38] through complex networks formed by grain boundaries. Models such as these can be used as subgrid constitutive models in large scale simulations, efficient surrogates for structure-property optimization and exploration, and in material variability quantification.

The key contributions of this paper are:

- We enable Bayesian UQ for GCNNs that emerge from two complex SciML applications of polycrystal stress response and out-gassing flux.
- We obtain the Bayesian UQ information by implementing and deploying SVGD and pSVGD to accommodate the GCNN architecture.
- We extract insights on the extremely narrow BNN posteriors resulting from the instability of NN model due to the underlying physics and time-integration requirements.

The paper is organized as follows. Sec. 2 provides an overview of the HMC, SVGD, and pSVGD algorithms used for conducting Bayesian inference of the NN parameters. Sec. 3 provides details the two SciML applications and their GCNN architectures. Sec. 4 then presents numerical results of the BNN construction from the different inference algorithms, along with the ensuing uncertainty information in the model and predictions. The paper concludes in Sec. 5 with a summary of the key findings and future work.

2 Methodology

NNs have seen success in representing processes with spatial-temporal complexity. A common approach combines two components: (a) a parameterized convolution for spatial dependence, and (b) a learnable recurrence relation for temporal evolution [39, 40, 41]. Thus, an input is first reduced to a latent description through convolutions, evolved by the recurrent component, and then decoded to the output space. For the spatial component, pixel-based convolutional neural networks (CNNs) operate on grid-structured data while graph-based CNNs (GCNNs) relax this requirement. Graph convolutions are flexible in the sense that they work equally well on the connectivity of structured grids and unstructured meshes, or on data that has a network relationship. For the temporal component, recurrent neural networks (RNNs) that describe time-integrator-like recurrent relations have seen wide application. These RNNs include specific architectures that target history-dependent processes such as the long short-term memory (LSTM) unit [42] and the gated recurrent unit (GRU) [43] that involve gating to form “long” and “short”-term memory. With similar goals, neural ordinary differential equations (NODEs) [44, 45] follow the well-known discrete time integrators of scientific computing [46, 47, 48] to learn a NN representation of the “right-hand-side” of ordinary differential equations (ODEs) describing the latent dynamics.

Generically, these models follow a three-part architecture:

$$\hat{y} = \text{NN}(X, f; w) = \begin{cases} h_0 & = \text{NN}_X(X; w_0) \\ h_{n+1} & = \text{NN}_h(h_n, f_n; w_n) \\ \hat{y}_n & = \text{NN}_y(h_n; w_y) \end{cases}. \quad (1)$$

First, the physical initial condition X is encoded into an initial hidden state h_0 , via encoder NN_X that is a convolutional NN with reduction via pooling. Then, the hidden state h_n , together with a time-like input f_n , is evolved in a time-integrating fashion by a RNN- or NODE-based NN_h . Finally, each hidden states is transformed to predict the output quantity of interest (QoI) \hat{y}_n via decoder NN_y , where the hat-notation indicates a *prediction* from the NN model. Collectively, we denote the entire time-trace quantities as $h := \{h_n\}_n$, $f := \{f_n\}_n$, and $\hat{y} := \{\hat{y}_n\}_n$. NN_X , NN_h , and NN_y are respectively parameterized by w_0 , w_n , and w_y , and similarly $w := \{w_0, w_y, \{w_n\}_n\}$ denotes the entire collection of weights for the model.

We explore NN_h in the forms of RNN and NODE. An RNN architecture resembles filters from control theory. For example, the particular form of a GRU update is

$$\begin{aligned} h_{n+1} = \text{NN}_h(h_n, f_n; w_n) &= (1 - z_{n+1}) \odot h_n + z_{n+1} \odot \tilde{h}_{n+1}, \\ &= h_n + z_{n+1} \odot (\tilde{h}_{n+1} - h_n), \end{aligned} \quad (2)$$

where \odot denotes the Hadamard element-wise product, and \tilde{h}_{n+1} is a trial state and z_{n+1} provides a gating mechanism on the update from h_n to h_{n+1} . Both the gate and trial state are computed by densely connected NNs on inputs f_n and h_n . The second form in Eq. (2) illustrates a resemblance of the gated RNN update with that of a discrete time integrator. A NODE is derived from time-integration of ODEs. For example, a forward Euler discretization of an underlying continuous-time ODE $\dot{h} = R(h, f)$ leads to

$$h_{n+1} = \text{NN}_h(h_n, f_n; w_n) = h_n + \Delta t R(h_n, f_n; w_n), \quad (3)$$

where Δt is the timestep.

Additional architecture details that are specific to the SciML applications will be presented in Sec.3.

2.1 Bayesian uncertainty quantification

A NN is trained using a training dataset of N_D time-traces: $\mathcal{D} = \{X_i, f_i, y_i\}_{i=1}^{N_D}$. An ordinary, non-probabilistic training involves optimizing the NN weight parameters to minimize some loss function that reflects the predictive capability of the overall NN model, for example $w^* = \arg \min_w \mathcal{L}(w; \mathcal{D})$. A common loss function is the mean-square error (MSE). In contrast, a Bayesian (probabilistic) training of the NN, resulting in a BNN, treats the weight parameters as a random vector that has an associated probability distribution. Given training data, Bayes' rule provides an update of the parameter distribution:

$$\pi(w | \mathcal{D}) = \frac{\pi(\mathcal{D} | w) \pi(w)}{\pi(\mathcal{D})} = \frac{\pi(\{y_i\}_i | \{X_i, f_i\}_i, w) \pi(w)}{\pi(\{y_i\}_i)}, \quad (4)$$

where $\pi(w)$ is the *prior* probability density that represents the uncertainty of NN parameters prior to considering the training data, $\pi(w | \mathcal{D})$ is the *posterior* probability density that represents the updated uncertainty of NN parameters after conditioning on data, $\pi(\mathcal{D} | w)$ is the *likelihood* that describes the probability of observing the data under a given parameter setting w , and $\pi(\mathcal{D})$ is the marginal likelihood (also called the model evidence) that does not depend on the parameters w . In the context of NNs, an uninformative independent normal distribution $\pi(w) \sim \mathcal{N}(\mathbf{0}, \sigma_0^2 \mathbf{I})$ is often adopted for the prior since many of the weights are fungible and have complex relationships with the physical outputs.

More precisely, the likelihood that is actually being computed is $\pi(\{y_i\}_i | \{X_i, f_i\}_i, w)$. It is usually established following an observation model (for all y_n in each time-trace) in the form $y_{i,n} = \hat{y}_{i,n}(X_i, f_i, w) + \epsilon_{i,n}$ where $\epsilon_{i,n} \sim \mathcal{N}(0, \sigma_\epsilon^2)$ is an independent Gaussian discrepancy with σ_ϵ reflecting the level of data noise. The independence of $\epsilon_{i,n}$ allows the joint likelihood to be decomposable into product of marginals: $\pi(\{y_i\}_i | \{X_i, f_i\}_i, w) = \prod_{i,n} \pi(y_{i,n} | X_i, f_i, w)$.

We will introduce the specific methods for computing the posterior $\pi(w | \mathcal{D})$ in subsections below. Once the posterior is obtained, one can then use the resulting BNN to obtain a corresponding distribution of predictions under given new input X^{new} and f^{new} , through the *posterior push-forward* distribution

$$\pi(\hat{y}^{\text{new}} | X^{\text{new}}, f^{\text{new}}, \mathcal{D}) = \pi(\text{NN}(X^{\text{new}}, f^{\text{new}}; w) | X^{\text{new}}, f^{\text{new}}, \mathcal{D}) \quad (5)$$

and the *posterior-predictive* distribution

$$\pi(y^{\text{new}} | \mathcal{X}^{\text{new}}, f^{\text{new}}, \mathcal{D}) = \int \pi(y^{\text{new}} | \mathcal{X}^{\text{new}}, f^{\text{new}}, \mathbf{w}) \pi(\mathbf{w} | \mathcal{D}) d\mathbf{w}. \quad (6)$$

The key difference is that the push-forward distribution simply propagates the parameter uncertainty through the NN and provides a distribution of NN predictions \hat{y} , while the predictive distribution also incorporates data noise in its overall uncertainty (e.g., the posterior predictive for the additive Gaussian observation model case is $\pi(y^{\text{new}} | \mathcal{X}^{\text{new}}, f^{\text{new}}, \mathcal{D}) = \pi(\text{NN}(\mathcal{X}^{\text{new}}, f^{\text{new}}, \mathbf{w}) + \epsilon | \mathcal{X}^{\text{new}}, f^{\text{new}}, \mathcal{D})$). Both distributions can be sampled by, for example, first generating samples $w_{(i)}$ from the posterior $\pi(\mathbf{w} | \mathcal{D})$, evaluating the NN model for each sample to obtain a corresponding sample of $\hat{y}_{(i)}^{\text{new}}$, and then adding a noise sample $\epsilon_{(i)}$ to obtain a sample of $y_{(i)}^{\text{new}}$. In this work, we will mostly study posterior push-forward behavior.

2.1.1 Hamiltonian Monte Carlo

Hamiltonian Monte Carlo (HMC) [25, 19] is an effective sampling algorithm in the Markov Chain Monte Carlo (MCMC) family. HMC frames the posterior sampling in terms of Hamiltonian dynamics (HD) evolution of the weights coupled with periodic Metropolis-Hastings (MH) steps [49]. HD allows the weights to transition away from the previous accepted state while staying in regions of high posterior probability, as a result of phase volume-preserving properties of HD. The usual MH acceptance criterion can then be applied to these decorrelated samples. The overall algorithm has some similarity to the thermostatted dynamics of single particle in a high dimensional space.

The Hamiltonian is comprised of a potential and a kinetic energy term:

$$H = \Phi + \frac{1}{2} \mathbf{p} \cdot \mathbf{M} \mathbf{p}. \quad (7)$$

The posterior $\pi(\mathbf{w} | \mathcal{D})$ is associated with the potential Φ via

$$\Phi = -\log \pi(\mathbf{w} | \mathcal{D}) \quad (8)$$

and the (fictitious) momentum \mathbf{p} is combined with a selected mass matrix \mathbf{M} to form a quadratic kinetic energy. The choice of the mass matrix effectively transforms the target parameter space by changing the constant H level sets and the correlation structure of the target distribution in terms of (\mathbf{w}, \mathbf{p}) . The choice of the form of kinetic energy is relatively free since the main requirement is that the probability distribution on the phase space marginalizes to the target distribution.

Computationally, HD is implemented with a symplectic (reversible, phase volume-preserving) integrator such as leapfrog Verlet:

$$\begin{aligned} \mathbf{p}_k((\tilde{n} + 1/2)\Delta t) &= \mathbf{p}_k(\tilde{n}\Delta t) - \frac{1}{2}\Delta t \nabla \Phi(\mathbf{w}_k) \\ \mathbf{w}_k((\tilde{n} + 1)\Delta t) &= \mathbf{w}_k(\tilde{n}\Delta t) + \Delta t \mathbf{M}^{-1} \mathbf{p}_k((\tilde{n} + 1/2)\Delta t) \\ \mathbf{p}_k((\tilde{n} + 1)\Delta t) &= \mathbf{p}_k((\tilde{n} + 1/2)\Delta t) - \frac{1}{2}\Delta t \nabla \Phi(\mathbf{w}_k((\tilde{n} + 1)\Delta t)), \end{aligned} \quad (9)$$

where k indexes the HD stage and \tilde{n} indexes pseudo-time of the HD trajectory. The time-integration generally requires the gradient of the log posterior with respect to the weights, which can make HMC computationally expensive relative to simpler MC methods. The effect of the mass matrix \mathbf{M} is evident from how it enters Eq. (9), by transforming \mathbf{p}_k and the effect of $\nabla \Phi$ on \mathbf{w}_k . The pseudo-time step Δt is chosen to maintain dynamic stability while promoting efficient decorrelation of states. The momentum provides a stochastic contribution to the overall dynamics: the initial momentum at stage k is a blend of the momentum from the previous HD stage plus a random component,

$$\mathbf{p}_k(0) = \beta \mathbf{p}_{k-1} + (1 - \beta) \boldsymbol{\varepsilon} \quad \text{with} \quad \boldsymbol{\varepsilon} \sim \mathcal{N}(\mathbf{0}, \mathbf{M}), \quad (10)$$

where β is a hyperparameter and $\mathbf{p}_0 = \boldsymbol{\varepsilon}$ for the first stage.

Lastly, the MH step for accepting the sample at each HMC stage k is carried out after integrating N_{MH} pseudo-time steps:

$$\mathbf{w}_{k+1} | \mathbf{w}_k = \begin{cases} \mathbf{w}_k(N_{\text{MH}}\Delta t) & \text{with probability } \alpha \\ \mathbf{w}_k(0) & \text{else} \end{cases}, \quad (11)$$

where the acceptance probability of the time-integrated value $\mathbf{w}_k(N_{\text{MH}}\Delta t)$ is

$$\alpha = \min \left(1, \frac{\exp(-H(N_{\text{MH}}\Delta t))}{\exp(-H(0))} \right). \quad (12)$$

The MH and the momentum initialization allow the overall chain to jump to new level sets of the Hamiltonian.

2.1.2 Stein variational gradient descent

Here we briefly review SVGD [31] and pSVG [34] methods that provide a coordinated ensemble of parameter samples through a type of functional gradient descent.

The methods are based on the Stein identity

$$\mathbb{E}_{\mathbf{x} \sim \pi}[\mathcal{A}_\pi[\phi(\mathbf{x})]] = \mathbf{0} \quad (13)$$

for a smooth function ϕ , where the operator \mathcal{A}_π is

$$\mathcal{A}_\pi[\phi(\mathbf{x})] = \nabla_{\mathbf{x}}[\log \pi(\mathbf{x})] \otimes \phi(\mathbf{x}) + \nabla_{\mathbf{x}}\phi(\mathbf{x}) \quad (14)$$

for a generic probability density $\pi(\mathbf{x})$. Notably, the Stein operator \mathcal{A}_π depends on the density π only through the *score* function $\nabla_{\mathbf{x}}[\log \pi(\mathbf{x})]$ which is independent of the normalization of π and thus is suitable for Bayesian inference where only the unnormalized posterior is available (i.e., having only access to prior times likelihood). If we let $\tilde{\pi}$ be an approximate density under a perturbation mapping of the random variable $\mathbf{x} \mapsto \mathbf{x} + \epsilon\phi$, then the expectation of $\text{tr}(\mathcal{A}_\pi[\phi(\mathbf{x})])$ can be shown to relate to the gradient of the Kullback–Leibler (KL) divergence between $\tilde{\pi}$ and π [31, Thm 3.1]:

$$\nabla_{\epsilon} D_{\text{KL}}(\tilde{\pi}_{\mathbf{x}+\epsilon\phi} || \pi)|_{\epsilon=0} = -\mathbb{E}_{\tilde{\pi}}[\text{tr}(\mathcal{A}_\pi[\phi(\mathbf{x})])]. \quad (15)$$

This connection provides the basis for a gradient-based method to update the approximate posterior density to the true posterior density.

Leveraging these relationships and with some additional derivations (see Ref. [31] for details), the SVGD algorithm initializes an ensemble of N_p particles $\{\mathbf{w}_{(i)}\}_{i=1}^{N_p}$ in the parameter space and updates them via gradient-descent steps

$$\mathbf{w}_{(i)}^{k+1} = \mathbf{w}_{(i)}^k + \gamma \mathbf{g}(\mathbf{w}_{(i)}^k), \quad (16)$$

where γ is a learning rate parameter and

$$\mathbf{g}(\mathbf{w}) = \frac{1}{N_p} \sum_{j=1}^{N_p} k(\mathbf{w}_{(j)}^k, \mathbf{w}) \nabla_{\mathbf{w}_{(j)}^k} [\log \pi(\mathbf{w}_{(j)}^k | \mathcal{D})] + \nabla_{\mathbf{w}_{(j)}^k} k(\mathbf{w}_{(j)}^k, \mathbf{w}) \quad (17)$$

is a gradient estimate. The kernel $k(\cdot, \cdot)$ is required to have certain regularity conditions, which can be satisfied by the radial basis function (RBF) kernel $k(\mathbf{w}, \mathbf{w}') = \exp(-\frac{1}{h} \|\mathbf{w} - \mathbf{w}'\|^2)$ for example [31]. Discussions on additional choices of the kernel, as well as incorporating gradient and approximate Hessian information into the kernel construction, can be found in Ref. [50]. Eq. (17) can be interpreted as a kernel-smoothed gradient that drives the particles toward the high-probability region of the posterior, and a repulsion term that keeps the particles separate. At convergence, the particles collectively approximate the posterior distribution.

2.1.3 Projected Stein variational gradient descent

SVGD has been observed to have a tendency for the particles to collapsing toward the maximum a posteriori (MAP) point (i.e., posterior mode) when the dimension of the parameter space, N_w , is much greater than the number of particles, N_p [32], which in turn underestimates the uncertainty in these situations. pSVG [34] combats this phenomenon by seeking to perform Bayesian inference only a lower-dimensional active subspace of the full parameter space. This subspace is based on the likelihood Hessian

$$\mathbf{H} = \nabla_{\mathbf{w}} [\nabla_{\mathbf{w}} \pi(\mathbf{y} | \mathbf{X}, \mathbf{f}, \mathbf{w})] \quad (18)$$

at the MAP, either in its full form or its Gauss-Newton first derivative approximation. The subspace is constructed from the r most significant generalized eigenvectors obtained from

$$\mathbf{H}\psi_l = \lambda_l \Sigma_0^{-1} \psi_l, \quad (19)$$

where Σ_0 is the prior covariance. The potentially large dimension eigenvalue problem can be efficiently solved by randomized numerical linear algebra [51]. The column matrix of the leading r eigenvectors, $\Psi = [\psi_0, \dots, \psi_r]$, allows the projection of parameters into the active low-dimensional subspace where the likelihood (data) highly informs the posterior:

$$\begin{aligned} \mathbf{w} &= \mathbf{w} - \bar{\mathbf{w}} + \bar{\mathbf{w}} \\ &= \underbrace{\mathbf{P}[\mathbf{w} - \bar{\mathbf{w}}]}_{\mathbf{w}^r} + \underbrace{\mathbf{Q}[\mathbf{w} - \bar{\mathbf{w}}] + \bar{\mathbf{w}}}_{\mathbf{w}^\perp}, \end{aligned} \quad (20)$$

where w^r is in the active subspace component, w^\perp is the inactive complement where the prior is dominant, and \bar{w} is the particle mean (or, alternatively, the MAP). Hence, $P = \Psi\Psi^\top$ is the projector to the active space and $Q = I - P$ is its complement.

The weights in the inactive subspace, which are considered as the unmodified prior’s projections, can be frozen at the samples of the prior. Then, the pSVG algorithm needs only to determine the posterior distribution in the lower-dimensional active subspace. Bayes’ theorem in the split parameter space becomes

$$\begin{aligned}\pi(w | \mathcal{D}) &\propto \pi(\{y_i\} | \{X_i, f_i\}_i, w) \pi_0(w) \\ &\approx \pi(\{y_i\} | \{X_i, f_i\}_i, w^r) \pi_0^r(w^r) \pi_0^\perp(w^\perp)\end{aligned}\quad (21)$$

where we assume an independent prior for the parameter subspaces, i.e., $\pi_0 = \pi_0^r \pi_0^\perp$. The log-posterior gradient in Eq. (17) is now replaced by the projected gradient

$$\nabla_{w_{(j)}^r} \log \pi(w_{(j)}^r | \mathcal{D}) = \Psi^\top \nabla_{w_{(j)}} \log \pi(w_{(j)} | \mathcal{D}).\quad (22)$$

The full-dimensional posterior is then reconstructed by mapping the low-dimensional samples $w_{(i)}^r$ back to its low-rank form and recombining it with the inert parts of the prior to yield a full rank approximation:

$$w_{(i)} = \Psi w_{(i)}^r + \bar{w} + w_{(i)}^\perp.\quad (23)$$

2.2 Illustrative comparisons of HMC, SVGD, and pSVG

We conduct two simple benchmark tests to compare HMC, SVGD, and pSVG. In both cases the likelihood associated with the data informing the third parameter component w_3 has high noise/low precision, and hence does not inform w_3 . Thus the posterior in that dimension remains close to the prior.

The first example involves a 3-dimensional multivariate Gaussian posterior illustrated in Fig. 1. pSVG thus truncates the last parameter dimension w_3 and only performs inference on the two informed active directions w_1 - w_2 . This example illustrates that for a well-behaved/convex posterior the SVGD samples are more structured than HMC having outer shells influenced by the repulsive part of the Stein potential and an inner density region dominated by the posterior density. The projected SVGD largely resemble those of SVGD, albeit with less structure/variance in the less precise w_3 dimension. All methods show convergence of their sample statistics to the those of the true posterior. The results in the right frame represent the first two diffusion map [52, 53] eigenvectors constructed with the HMC samples. The wider region in the center correspond the bulk of the samples near the center of the distribution while the side tails correspond to the narrowing of the distribution towards the positive/negative w_3 values where the spread of (w_1, w_2) pairs shrinks in absolute sense.

The second example entails a highly non-Gaussian 3-dimensional posterior, as visualized in Fig. 1 using samples/particles from the three algorithms. This posterior shows a more complex connected set of high probability samples with adjacent MAPs connected by high density bridges, which we believe is qualitatively similar to that generated by nonlinear NNs with fungible weights. Clearly this is illustrative of strong non-linear correlation of the parameters. HMC and full SVGD represent the posterior well, with SVGD’s fewer samples spanning the likely parameters efficiently. Projected SVGD appears to be hampered by decoupling the dominant modes from the less dominant mode and is stuck sampling one of the many high probability posterior regions. Similarly, the right frame displays the diffusion map eigenvectors corresponding to the HMC results for this test case. The strong dependencies between all model parameters result in samples embedded in a circular manifold.

In this paper we will refer to possible multiple local maxima posterior distribution values as *local MAPs*, to keep the terminology concise. While this nomenclature can, in general, be confusing, in the context of this paper it is clear that we refer to local, possibly degenerate maxima of the posterior.

3 Scientific machine learning applications

We will demonstrate building BNNs using the methods in Sec.2 on two SciML applications featuring spatial-temporal complexity: (a) prediction of the stress response of polycrystals undergoing plastic deformation [4] modeled with a GCNN-RNN, and (b) prediction of the out-gassing flux of polycrystals with gas generation modeled with a GCNN-NODE. The underlying (data-generating) models are solutions to conservation equations on a regular domain and have a single QoI that evolves in time. We first describe the application background, data generation, and NN architecture in this section, and then present the BNN results in Sec.4.

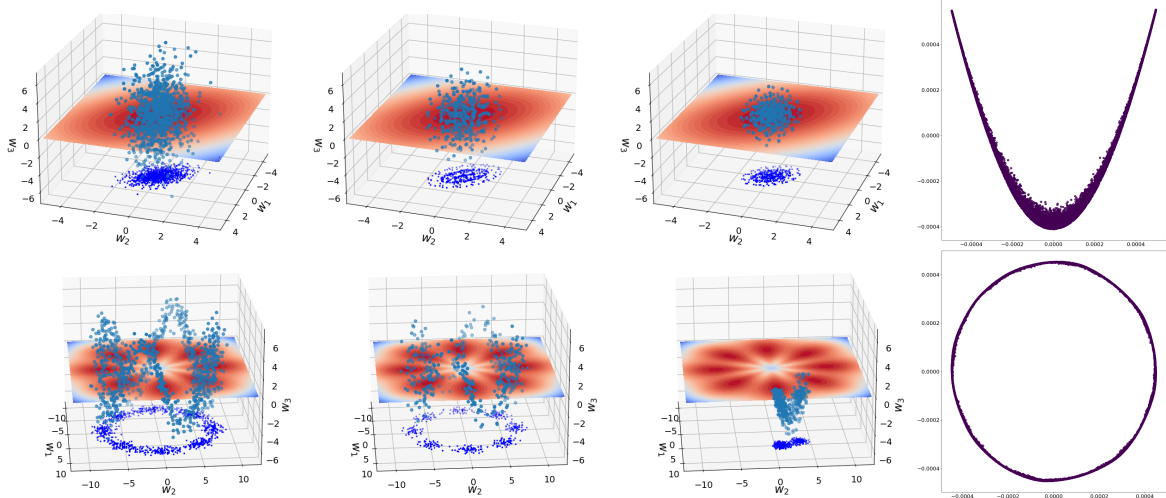


Figure 1: Illustration of likelihood and samples from HMC, SVGD, and pSVGd for MVN (upper row) and Tor (lower row). The base shows samples projected to the w_1 - w_2 plane. Left to right: HMC, SVGD, pSVGd, diffusion map eigenvectors.

3.1 Mechanical response of polycrystals

The deformation response of metal polycrystals underlies the phenomenological plasticity models that enable metal forming and crash analysis. Polycrystalline aggregates, where crystal plasticity governs the individual grain response, are a common target for homogenization in pursuit of sub-grid and structure-property surrogate models [54, 55, 56, 57, 4, 58]. These models help predict plastic deformation that can lead to structural failure.

3.1.1 Physical system

Each polycrystalline sample is a collection of convex sub-regions Ω_K of a square Ω_\square , and the number of Ω_K comprising the domain Ω_\square vary sample to sample. Each sub-region represents an individual crystal in the sample aggregate. The crystal lattice orientation distinguishes one crystal from another, which is characterized by the angle field $\phi(\mathbf{X})$, where \mathbf{X} is the position vector in the initial configuration of the polycrystal. For this exemplar, the angles are drawn from a uniform distribution, $\mathcal{U}[0, 2\pi]$.

In this application, the QoI is the time-varying average stress $\bar{\mathbf{S}}(t)$, which depends on deformation history. Crystal plasticity models [59, 60] are comprised of an algebraic relation mapping recoverable elastic strain to stress and a set of ODEs governing the evolution of irrecoverable plastic strain. The stress field $\mathbf{S} = \mathbf{S}(\mathbf{X}, t)$ is given by

$$\mathbf{S} = \mathbf{S}(\boldsymbol{\epsilon}_e) = \mathbb{C} : \boldsymbol{\epsilon}_e, \quad (24)$$

where \mathbb{C} is the 4th order elastic modulus tensor and $\boldsymbol{\epsilon}_e$ is elastic strain. In each sub-region Ω_K , the orientation vector ϕ rotates $\mathbb{C} = \mathbf{R}(\phi) \boxtimes \underline{\mathbb{C}}$ from the canonical $\underline{\mathbb{C}}$. Here \boxtimes is the Kronecker product:

$$\mathbf{R} \boxtimes [\mathbf{A}]_{ij\dots} \mathbf{e}_i \otimes \mathbf{e}_j \otimes \dots = [\mathbf{A}]_{ij\dots} \mathbf{R}\mathbf{e}_i \otimes \mathbf{R}\mathbf{e}_j \otimes \dots \quad (25)$$

We chose the common face centered cubic (FCC) symmetry for each crystal, which has three independent components of the elastic modulus tensor \mathbb{C} . In each crystal, plastic flow can occur on any of the 12 FCC slip planes defined by slip plane normals \mathbf{n}_α and slip directions \mathbf{s}_α , where $\mathbf{s}_\alpha \perp \mathbf{n}_\alpha$. The plastic velocity gradient, which determines the plastic strain

$$\mathbf{L}_p = \mathbf{L}_p(\mathbf{S}) = \sum_{\alpha} \dot{\gamma}_{\alpha}(\mathbf{S}) \mathbf{s}_{\alpha} \otimes \mathbf{n}_{\alpha} \quad (26)$$

is governed by slip rates $\dot{\gamma}_{\alpha}$, the rotated dyads $\mathbf{s}_{\alpha} \otimes \mathbf{n}_{\alpha} = \mathbf{R}(\phi) \boxtimes (\underline{\mathbf{s}}_{\alpha} \otimes \underline{\mathbf{n}}_{\alpha})$, and the stress \mathbf{S} at the particular location. The slip rate $\dot{\gamma}_{\alpha}$ follows a power law

$$\dot{\gamma}_{\alpha} = \dot{\gamma}_0 \left| \frac{\tau_{\alpha}}{g_{\alpha}} \right|^{m-1} \tau_{\alpha} \quad (27)$$

driven by the shear stress $\tau_{\alpha} = \mathbf{s}_{\alpha} \cdot \mathbf{S} \mathbf{n}_{\alpha}$ resolved on slip system α , while the slip resistance g_{α} evolves according to [61, 62]:

$$\dot{g}_{\alpha} = (H - R_d g_{\alpha}) \sum_{\alpha} |\dot{\gamma}_{\alpha}|. \quad (28)$$

Table 1 summarizes parameter descriptions and values.

Elastic moduli	C_{11}	1.000
	C_{12}	0.673
	C_{12}	0.617
Hardening modulus	H	0.00174
Initial slip resistance	g_α	0.000597
Applied strain rate	$\dot{\epsilon}$	1.000
Reference slip rate	$\dot{\gamma}_0$	1.000
Rate sensitivity exponent	m	20
Recovery constant	R_d	2.9

Table 1: Crystal plasticity parameters representative of steel. All moduli are made dimensionless by $C_{11} = 205$ GPa and all rates were non-dimensionalized by the applied strain rate $1s^{-1}$. The maximum strain attained by the simulations was 0.003. Note the moduli $[C]_{iiii} = C_{11}$, $[C]_{ijjj} = C_{12}$, and $[C]_{ijij} = C_{44}$, where $i \neq j$.

Fig. 2a shows 3 realizations of the orientation field ϕ on a 32×32 grid which differ in the grain topology and the orientation field defining the grain structure. For each sample the balance of linear momentum

$$\text{div } \mathbf{S} = \mathbf{0} \quad (29)$$

is solved for the displacement field using the finite element method, subject to tension at a strain rate of $1/s$ effected by minimal boundary conditions on the domain Ω_\square , i.e., two parallel boundaries and one corner are constrained. Fig. 2b illustrates the inhomogeneities in the stress response (at 0.3% strain in tension), which are particularly marked at grain boundaries. The overall response of samples reflects the anisotropy of each crystal which share boundaries and, hence, have kinematic constraints on their deformation. The resulting mean stress $\bar{\mathbf{S}}(t)$ response curves

$$\bar{\mathbf{S}}(t) = \frac{1}{V} \int_{\Omega} \mathbf{S} d^3X \quad (30)$$

are the final QoIs. They vary due to the particular texture $\phi(\mathbf{X})$ of the realization, where V is the volume of Ω_\square . In fact, the different crystal textures evoke different effective elastic slopes, yield points, and (post-peak) flow stresses as can be seen in Fig. 3.

3.1.2 Neural network architecture

The general NN architecture for this data has been published previously [2, 4] and is depicted in Fig. 4. The physical inputs are the orientation field $\phi(\mathbf{X})$ and the applied strain $\mathbf{f} = \bar{\epsilon}(t)$; the output is the mean stress over time $\mathbf{y} = \bar{\mathbf{S}}(t)$. The orientation field $\phi(\mathbf{X})$ is discretized on a mesh. The discrete values of the texture ϕ and the associated cell volume fractions ν comprise the nodal data $\mathbf{X} = [\phi, \nu]$ for the graph associated with discretization mesh. The nodal input data \mathbf{X} and the graph adjacency matrix A are fed into a convolutional stack. The GCNN layers have the form of the Kipf and Welling GCN [63] with an independent self weight. The result of this convolutional stack is pooled with global averaging to produce hidden features \mathbf{h}_0 that describe the factors that are salient to the prediction of the mean stress. One feature per filter is produced by the convolutional encoder. These features depend only on the initial microstructure as described by $\phi(\mathbf{X})$ and, hence, are time-independent. These hidden features \mathbf{h}_0 and the time dependent input $\mathbf{f} = \bar{\epsilon}(t)$ are concatenated and then fed into a GRU RNN [43] with the applied strain acting as \mathbf{f} . The output of this layer is fed to a linear dense decoder to produce $\hat{\mathbf{y}} = \bar{\mathbf{S}}(t)$. The entire model has a total of $N_w = 205$ parameters. Fig. 4 provides a schematic of the overall NN model with further details.

We will also employ a larger version of the model shown in Fig. 4 to demonstrate the performance of SVGD and pSVGd on a problem that is intractable to HMC. This GCNN-RNN model operates on three-dimensional data using 2 convolutional layers with 16 filters, 1 post pooling dense layer with *swish* activation, and 1 dense output layer. It has 2609 parameters total, with $112 + 528$ in the convolutions, $272 + 17$ in the dense layers, and 1680 in the GRU.

3.2 Diffusion and generation in polycrystals

Gas generation and diffusion in granular materials presents an engineering challenge in applications such as uranium fuel [37, 38]. Predictive modeling of out-gassing can avert catastrophic failures in nuclear power infrastructure. Here we reduce the learning problem to diffusion on graphs with a complex generation term.

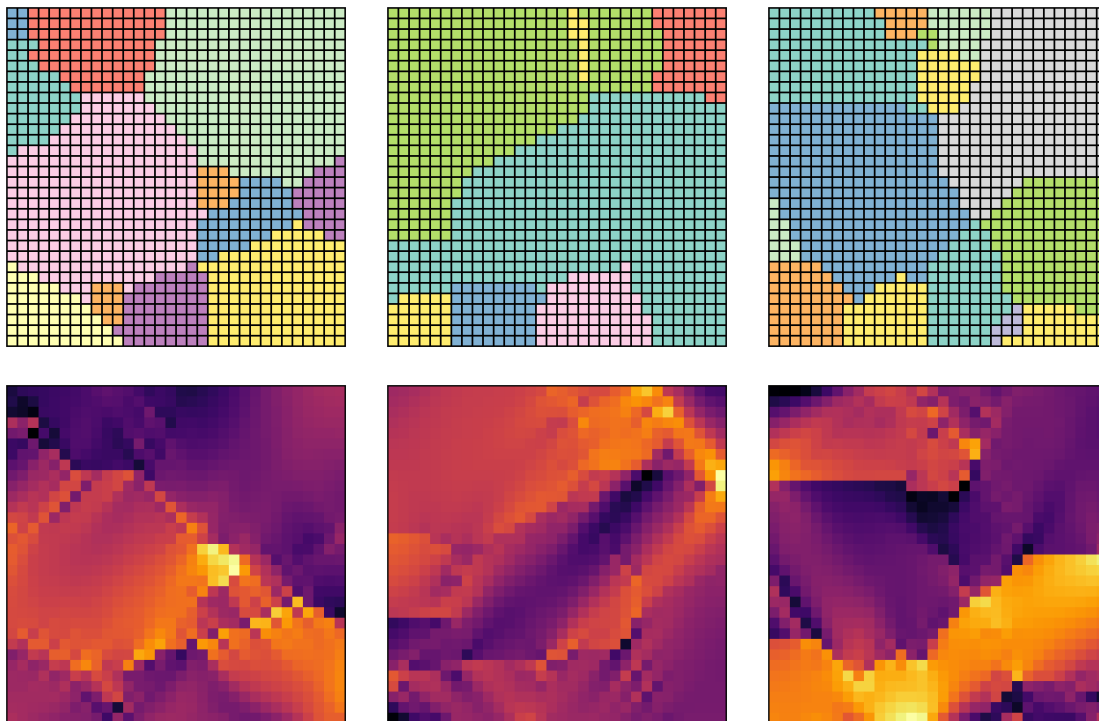


Figure 2: Crystal plasticity. Upper panel: realizations of the orientation field ϕ . Lower panel: corresponding S_{11} field at maximum applied tensile (ϵ_{11}) strain.

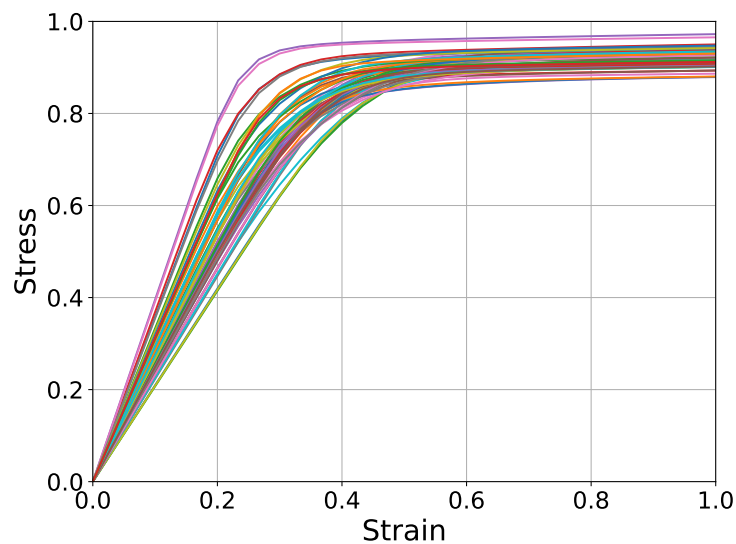


Figure 3: Crystal plasticity: normalized stress response curves $\bar{S}(t)$ for different configurational realizations ($\phi(\mathbf{X})$).

3.2.1 Physical system

Similar to the crystal plasticity exemplar, the domain Ω_{\square} consists of a square with convex subregions Ω_K which represent grains; see Fig. 5. Gas is generated in grains and slowly diffuses to the intergranular boundaries. The diffusion along the more disordered, looser atomically packed boundaries is relatively fast. This creates an intergranular network.

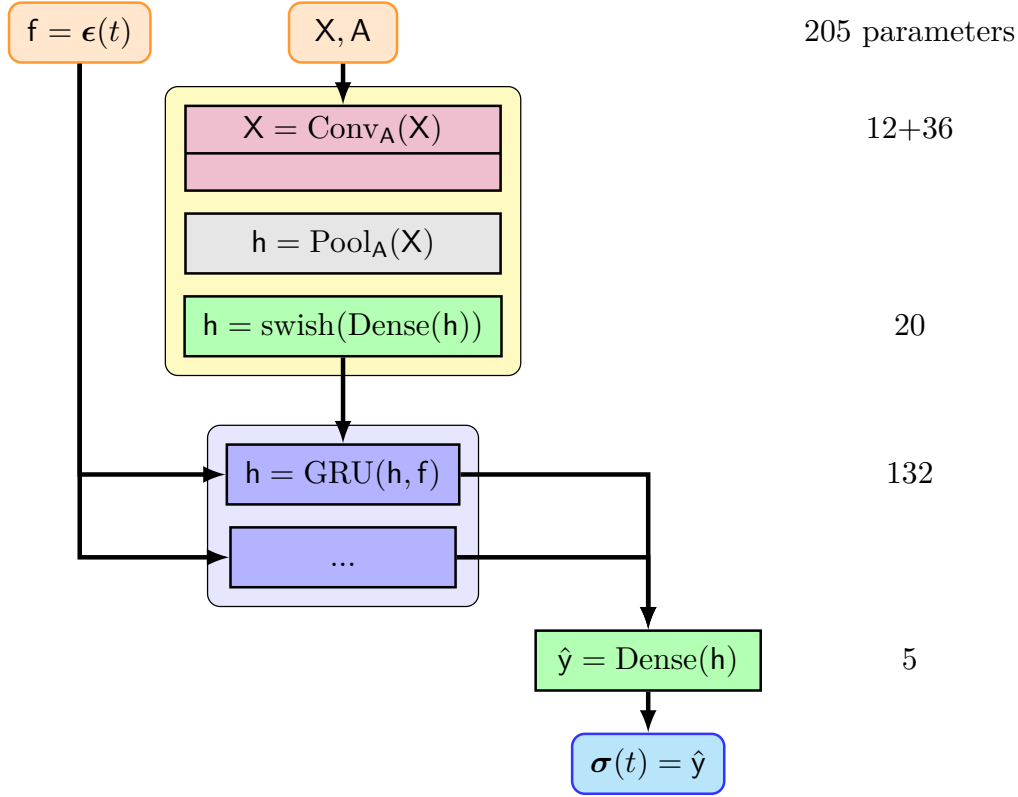


Figure 4: GCNN-GRU model of the crystal plasticity data, $N_w = 205$. The 2 convolutional layers have 4 filters each and *swish* activation. The GRU has *tanh* activation and is depicted as unrolled with a layer per time-step.

The coupled reaction-diffusion equations describing the concentration c are

$$\dot{c} = \text{div}(\kappa_b \nabla c) + \rho \quad \text{in } \Omega_K \quad (31)$$

$$\dot{c} = \text{div}(\kappa_s \nabla c) \quad \text{on } \partial\Omega_K \quad (32)$$

where κ_b is the bulk diffusivity, ρ is the gas generation and κ_s is the boundary diffusivity. Table 2 gives non-dimensional values for the parameters. With reference to Fig. 5, the boundary conditions are: the top and bottom are periodic, the left is open to out-gas, and the right boundary is closed. Initially there are gas concentrations at voids in the material as depicted in Fig. 5a. Fig. 5b shows the state of the extended system long after the initial conditions, and Fig. 6 shows the variety of flux response curves obtained via a finite volume method.

Intragrain gas generation	ρ	700.0
Intragrain gas diffusivity	κ_b	1.0
Grain boundary gas diffusivity	κ_s	1000.0

Table 2: Gas diffusion parameters representative of slow bulk diffusion and fast boundary diffusion, as in gas release from uranium fuel. All are made dimensionless using κ_b and the fact that the samples were in unit squares. The maximum time is set to 0.0005.

3.2.2 Neural network architecture

Given the relative time-scales of the bulk versus the boundary diffusion processes, we choose to reduce the problem to a model on the grain boundary network $\cup_K \partial\Omega_K$:

$$\dot{c} = \text{div}_G c + r(c) \quad (33)$$

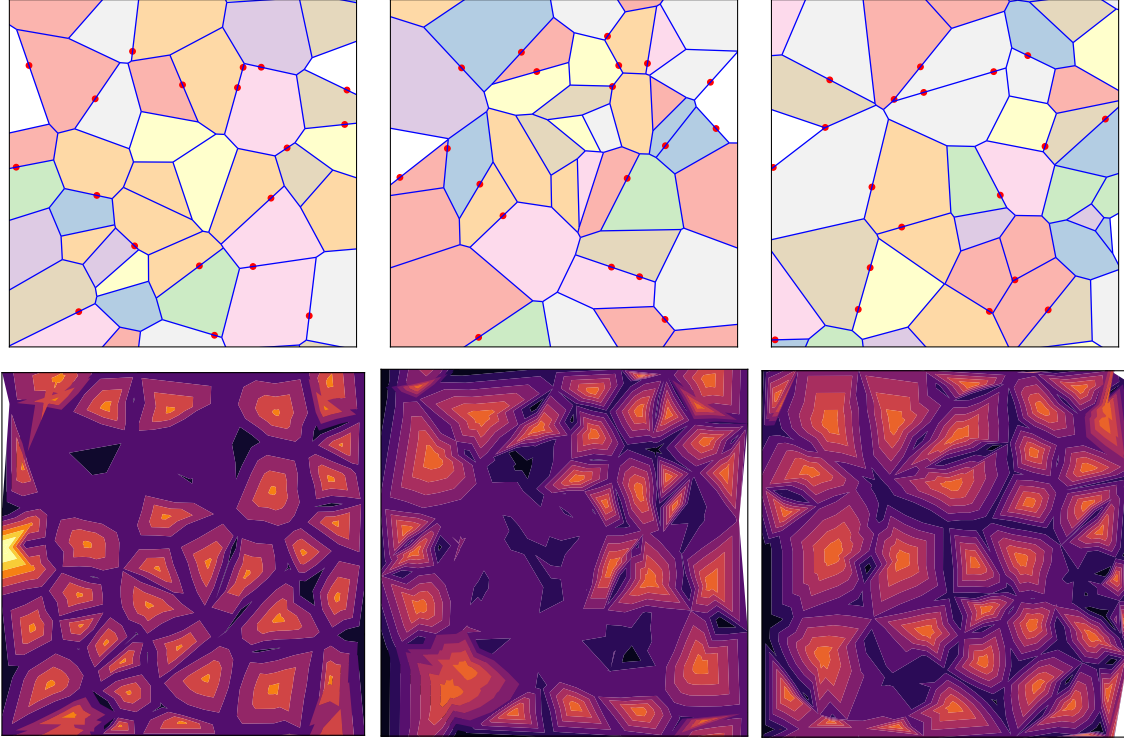


Figure 5: Gas release in polycrystalline systems. Upper panel: initial state, red dots represent bubbles in voids. Lower panel: gas concentration at $t = 0.0005$.

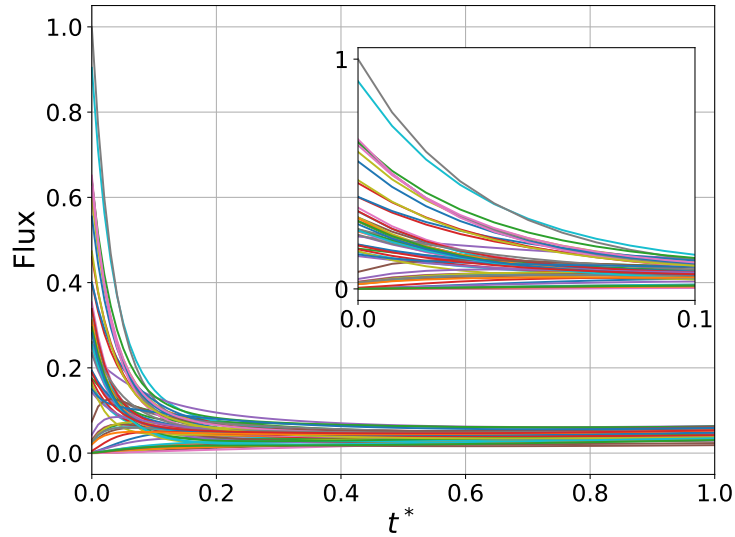


Figure 6: Gas release: normalized flux response curves for different configurational realizations.

where div_G is the divergence operator on a graph and the generation term is intended to represent the complex interaction of the boundary network with the gas-generating grains. After discretization, this system reduces to a system of ODEs with a linear-plus-nonlinear right-hand side:

$$\dot{c} = Kc + R(c, X) . \quad (34)$$

where c is the concentration on boundary network. Since the concentration field c in the grains is hidden from the network, we augment the concentration state with additional degrees of freedom to form the initial state X in the

style of an augmented NODE [44]. The augmented state is initialized with the nodal concentrations c at time $t = 0$, tributary areas ν (for bulk interactions), tributary lengths ℓ (for surface interactions), and zeros for additional states such that $\mathbf{X} = [c_0, \nu, \ell, 0, \dots]$ for every graph node, this information becomes the initial hidden state \mathbf{h} . Since there are no external influences on the system \mathbf{f} is simply a sequence of times.

The decomposition in Eq. (34) enables a physics informed treatment where we assume the form of the diffusion is defined by the graph describing the network and the generation term \mathbf{R} is completely data informed. The linear part of the right-hand side representing in-network diffusion is simply

$$\mathbf{K}c = \text{ReLU}(\kappa)\mathbf{L}c, \quad (35)$$

where $\mathbf{L} = \text{rowsum}(\mathbf{A}) - \mathbf{A}$ is the graph Laplacian, \mathbf{A} is the graph adjacency, and κ is a non-negative trainable parameter. The nonlinear term \mathbf{R} representing gas generation is modeled by graph convolutions so that the overall system is notionally

$$\dot{c} = \underbrace{\kappa \mathbf{L}}_{\mathbf{K}} c + \underbrace{\text{Conv} \mathbf{X}}_{\mathbf{R}(c, \mathbf{X})} \quad (36)$$

where Conv is a stack of convolutions and activations. The parameters of the convolutions Conv and κ are the learnable aspects of this hybrid NODE. Boundary conditions are imposed with penalization in \mathbf{L} and by projection with \mathbf{R} . The QoI y is flux of gas at the open boundary over time, which is obtained by selective pooling of \mathbf{h} .

The form of Eq. (34) suggests a classical fractional-step/operator-split [64, 65, 66] time integration. For the linear part we employ an exponential integrator. For the nonlinear part we employ a forward Euler update, although backwards Euler, midpoint, etc. can also be utilized. The complete time integration scheme for the concentrations c and hidden variables is:

$$\begin{aligned} c_{n+1/2} &= \exp(1/2\Delta t \mathbf{K}) c_n \\ \mathbf{h}_{n+1} &= \mathbf{h}_n + \Delta t \mathbf{R}(\mathbf{h}_n) \\ c_{n+1} &= \exp(1/2\Delta t \mathbf{K}) c_{n+1/2} \end{aligned} \quad (37)$$

with the hidden state vector \mathbf{h} subsuming the (hidden) concentration state $\mathbf{h} = [c, \dots]$, and with slight abuse of notation $\mathbf{R}(\mathbf{h})$ is the learnable function emulating $\mathbf{R}(c, \mathbf{X})$.

The hybrid NODE model is depicted in Fig. 7, which also contains additional details of the architecture such as depth of the convolutional stack, activations, and number of filters. Note that the time-scaling of the NODE allows for training strategies such as training to an increasing sequence of history or training to a coarse-then-fine version of the history to ease training to the full history.

3.3 Sampling and training

In this section we describe implementation details of our methods and hyperparameter choices.

The MAP, which are needed for initializing the particles in SVGD and pSVG, are found using the Adam optimizer [67] with early stopping. In all numerical examples, we employ a prior to be $\pi(\mathbf{w}) \sim \mathcal{N}(\mathbf{0}, \sigma_0^2 \mathbf{I})$ with $\sigma_0 = 1$. The NN parameter prior's standard deviation of $\sigma = 1$ is sufficiently large to be uninformative compared to the range $\mathcal{O}(10^{-2})$ to $\mathcal{O}(10^{-1})$ eventually explored by the NN parameters. The likelihood follows an observation model described in Sec. 2.1: $y_{i,n} = \hat{y}_{i,n}(\mathbf{X}_i, \mathbf{f}_i, \mathbf{w}) + \epsilon_{i,n}$ with independent Gaussian noise $\epsilon_{i,n} \sim \mathcal{N}(0, \sigma_\epsilon^2)$. The data noise is set to $\sigma_\epsilon = 0.05$ for the crystal plasticity data and $\sigma_\epsilon = 0.02$ for the gas flux data. All values of \mathbf{X} , \mathbf{f} , \mathbf{y} are normalized to the range $[0, 1]$ using their corresponding minimum and maximum instances from the training dataset.

To boost efficiency of HMC in terms of computational time and memory when handling the larger datasets, gradient evaluation of the likelihood, Eq. (8), is approximated by using a random subset of the full training dataset and proportionally scaled up by the number of data points. This subset is resampled at every evaluation. This procedure can be seen as a form of pseudo-marginal subsampling [68].

The SVGD initializes N_p particles at the MAP plus some jitter to make them distinct. We adopt a weighted RBF kernel

$$k(\mathbf{w}, \mathbf{w}') = \exp\left(-\frac{1}{h} \|\mathbf{w} - \mathbf{w}'\|_{\tilde{\mathbf{H}}}^2\right), \quad (38)$$

where $\tilde{\mathbf{H}}$ is an approximate Hessian matrix and h is the bandwidth. We select an adaptive bandwidth $h = \bar{d}^2 / \log N_p$ where \bar{d} is the median pair-wise distance between particles. pSVG use the same initialization and employs a tolerance on the eigenvalues of the Hessian to construct a subspace from its eigenvectors. The Hessian-based reductions are done layer-wise to prevent disconnected networks.

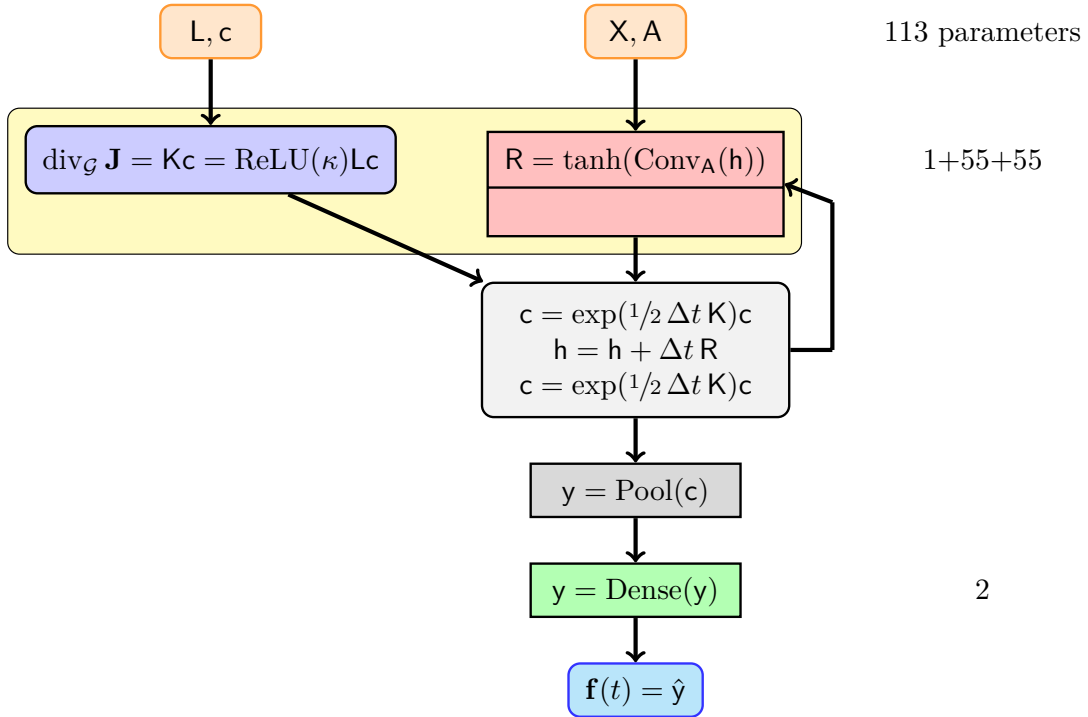


Figure 7: Hybrid NODE-GCNN architecture for gas release. Each convolutional layer has 5 filters which is also the size of the augmented state X .

4 Results

In this section, we first use the two-dimensional (2D) NN models described in Sec.3 to compare SVGD with HMC, which we treat as the reference baseline. We then use the larger three-dimensional (3D) NN models to explore the performance of pSVGD and comparing with SVGD, for a problem size that is currently infeasible for HMC.

The exemplar NN models described in Sec.3 are similar in that they all predict the evolution of a global QoI based on an initial spatial configuration. In terms of parameters, the RNN-based model of plasticity (Sec. 3.1) has many parameters in the GRU, while the NODE model of diffusion (Sec. 3.2) has relatively more parameters in the graph convolutions than in the time integration. Furthermore, the diffusion model has a physics-informed plus learned discrepancy formulation with a component with known form, the diffusion, and the learned part, the generation, and hence is more constrained than the GCNN-RNN. The GRU effectively has the same initial conditions, see Fig. 3, while the NODE has a wide variety, see Fig. 6. For the GRU model of plasticity, the hardest feature to capture is the transition from elastic to fully plastic flow, while the NODE has the task of correlating the graph structures and bubble locations with the variety of initial conditions. Both formulations can have stability issues predicting the evolving processes.

4.1 Comparison of SVGD and HMC

In this section we compare the UQ results provided by SVGD and HMC for the two exemplars. Since many NNs tend to be over-parameterized, we examine two cases of different training data sizes: (a) $N_D = \frac{1}{2}N_w$ with the number of samples being half the number of parameters, and (b) $N_D = 2N_w$ with the number of samples being twice the number of parameters. For SVGD we use $N_p = 96$ particles, which is on par with the number of parameters.

Fig. 8 shows traces of HMC chains for the crystal plasticity exemplar problem modeled with a GCNN-GRU. While each 2D slice individually would suggest the chains cover the same parameter region, it turns out that each set of results explore a separate region when inspecting chains across several slices of the parameter space. Each individual chain, either starting from a common MAP value (in the left frame) or starting from multiple MAP values (in the right frame) exhibit a high degree of autocorrelation induced by the seemingly non-convex posterior distribution. Recall

that these MAP values are found using gradient-based numerical optimization algorithms, and thus may correspond to different *local* MAP values (i.e., from local minima). Results for the NODE-based model are similar to the GRU-based results shown in Fig. 8. While the HMC stepsize and number of steps were adapted to obtain reasonable acceptance rates and stable NN models, further attempts to alleviate the degree of autocorrelation have not been successful.

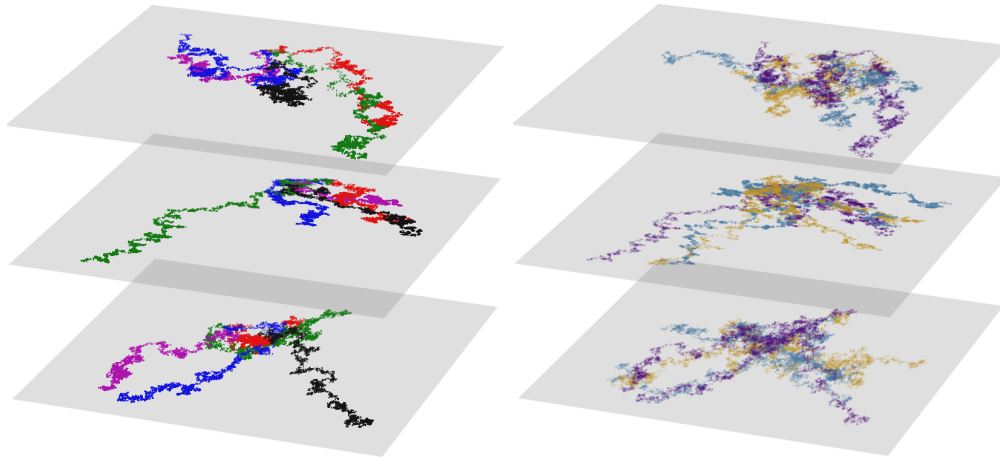


Figure 8: HMC chain traces plotted in two parameter components for the GRU model showing the dynamics for several parameter pairs. Left frame shows chain samples that start at the same MAP value, with different random number generator seeds. The right frame shows samples obtained from chains initialized from different MAP values. Results were thinned out (shown every 10^3 samples) for clarity.

Fig. 9 shows low-dimensional representations of the chains used to construct the 2D slices in Fig. 8. The left panel depicts 3D t-SNE representations [69] of chains starting from the same local MAP value, shown with a black circle. This dimensionality reduction technique clusters high-dimensional samples onto a lower dimensional space by minimizing the Kullback-Liebler divergence between probabilities that define the degree of similarity between samples in the high- and the low-dimensional spaces, respectively. The reduction to a 3D space, in the right panel, shows HMC paths that do not mix, consistent with the chain traces illustrated in Fig. 8. The right frames shows low-dimensional representations obtained via Laplacian eigenmaps [70] constructed using pair-wise distances between HMC samples. This dimensionality reduction technique is similar to the the diffusion map framework employed in Sec. 2.2 for the canonical distribution samples. The Laplacian eigenmap shows the components of the eigenvectors corresponding to the largest three eigenvalues of the Laplacian matrix. The eigenvectors corresponding to the four chains exhibit a similar structure when analyzed independently which indicate that chain evolve along a narrow high posterior region but never return to the starting point or any region previously visited.

We next employ the distance correlation [71, 72] to measure the degree of dependence between subsets of parameters in the GRU and NODE models. By construction, distance correlation can be applied to random variables of different dimensionality. Table 3 and Table 4 give the distance correlation between the weight ensembles grouped by layer. The entries in these tables are ranges covering simulations starting from several MAP values. For GRU, all layer parameters are highly dependent, with the output having a slight increasing trend from input convolution (*GCNN1*) to the pre-output dense layer. The correlations for NODE on the other hand, show that the graph convolutions are strongly dependent (the bold entries in the table) and work together to represent the complex generation behavior. These layers are only loosely correlated with the single parameter (*Scale*) used in the diffusion component and with the output layer. The NODE also shows increasing dependence of the layers from input to output with the output layer, albeit much weaker compared to the GRU model.

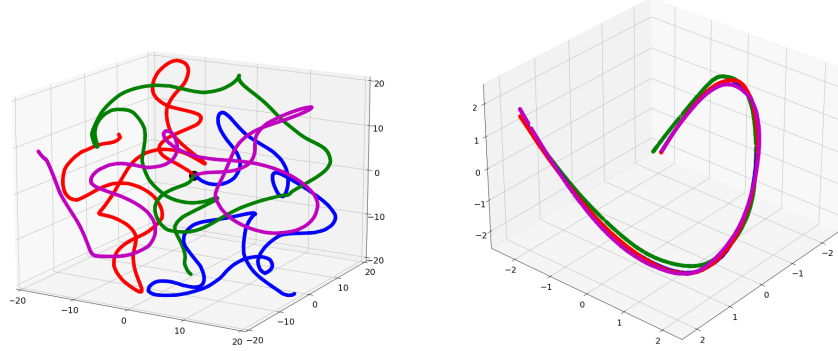


Figure 9: GRU: Low-dimensional embeddings for the HMC chains corresponding to the case using $N_d = \frac{1}{2}N_w$. Results correspond to 4 chains with different random seeds, all starting from the same MAP value (location shown with black circle in the left frame). The left frame shows data processed with the T-SNE algorithm; the right frame shows results generated via spectral embedding.

	GCNN1	GCNN2	Dense	GRU	GCNN1	GCNN2	Dense	GRU
GCNN2	0.90–0.94				0.92–0.93			
Dense	0.91–0.92	0.93–0.96			0.91–0.94	0.93–0.96		
GRU	0.92–0.94	0.97–0.98	0.95–0.98		0.91–0.93	0.96–0.97	0.96–0.97	
Output	0.72–0.73	0.78–0.83	0.81–0.85	0.81–0.85	0.58–0.83	0.75–0.85	0.75–0.89	0.78–0.89

Table 3: Distance correlation values for the HMC-based inference using the GRU model and $N_D = 105$ (left) and $N_D = 420$ (right) data samples.

	Scale	GCNN1	GCNN2	Scale	GCNN1	GCNN2
GCNN1	0.54–0.71	-	-	0.55–0.79	-	-
GCNN2	0.50–0.69	0.97–0.98	-	0.55–0.69	0.96–0.98	-
Dense	0.15–0.24	0.22–0.47	0.23–0.45	0.14–0.30	0.20–0.25	0.21–0.27

Table 4: Distance correlation values for the HMC-based inference using the NODE model and $N_D = 60$ (left) and $N_D = 240$ (right) data samples.

Fig. 10 and Fig. 11 show the GCNN-RNN and GCNN-NODE model predictions of the QoI made at the MAP realization w_{MAP} , for three cases corresponding to minimum, median, maximum MAP discrepancy from the entire dataset. We define the MAP discrepancy, for the i th data sample, as the root-mean square error (over all time steps in the time trace) between the MAP prediction compared to the corresponding data sample:

$$\|y_i - \text{NN}(X_i, f_i; w_{\text{MAP}})\|_{\text{RMSE}}. \quad (39)$$

The colormap indicates higher probability with darker shades near the median of the PF distribution. The grey lines correspond to the 5% and 95% quantile levels. The solid blue line indicating the MAP PF should generally overlap with the darker blue region. Nevertheless, in this case, as the posterior distribution is highly irregular, different chain discover adjacent local minima, giving rise to the discrepancy between the initial condition for these HMC chains and the bulk of the subsequent samples. The confidence bands of the PFs show some signature of uncertainty growing in time and being largest where there is the most variance in the data. The confidence bands also show that SVGD appears to better cover the data; however, the HMC and SVGD predictions are more comparable when the entire dataset is taken into account, as shown in Fig. 12.

Fig. 12 illustrates the similarity between (a) HMC versus observed data, (b) SVGD versus observed data, and (c) HMC versus SVGD results, over time. We use the Kolmogorov-Smirnov statistic (KSS) to measure the similarity of two cumulative distribution functions (CDFs):

$$\text{KSS}(\text{CDF}_1, \text{CDF}_2) = \int_{-\infty}^{\infty} |\text{CDF}_2(y) - \text{CDF}_1(y)| dy, \quad (40)$$

where we approximate the CDFs with the empirical CDFs constructed with the posterior push-forward distributions using samples from the HMC chains and SVGD particles, respectively. To facilitate the comparison of a posterior push-forward with data, we use a Heaviside function centered at the data value y as the data CDF. These statistics also

show the signatures of the variance of the output features through time. Similarities between the predictions and the data are good throughout time but are more dissimilar (higher KSS) in the highly variable, hard to predict regimes. The highly variable plastic transition in the region of $[0.1, 0.4]$, where the elastic-plastic transition occurs, is seen in the GRU similarity scores, while the variance of the initial conditions is seen in the NODE similarity scores.

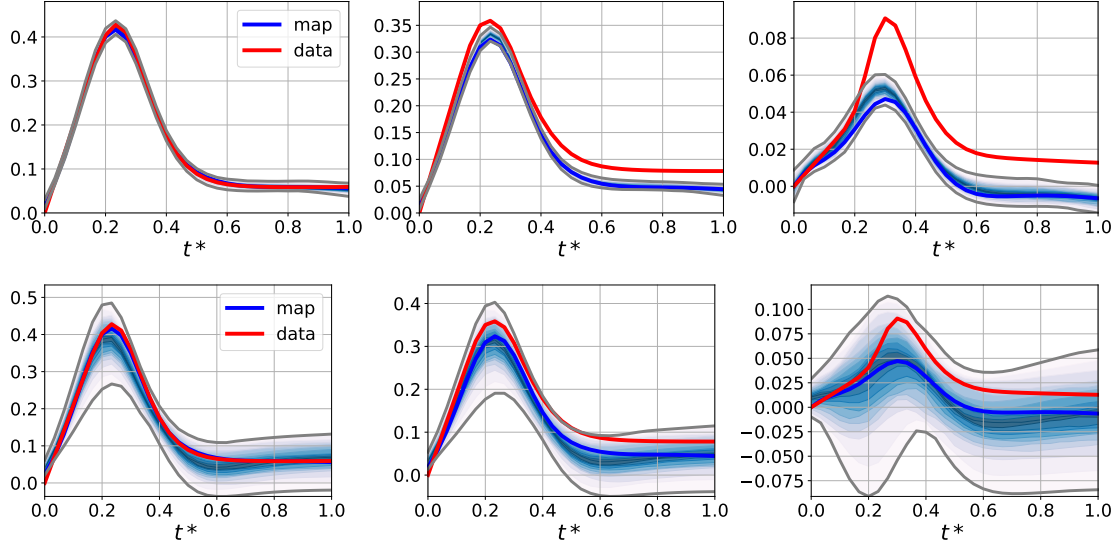


Figure 10: RNN: Three cases corresponding to minimum (left), median (middle), maximum (right) MAP discrepancy for training with $N_D = \frac{1}{2}N_w$ data points. Each plot show the MAP prediction, posterior push-forward distribution, and the corresponding data sample. Top row shows HMC results and bottom row shows SVGD results. Note the change in vertical scale from left panels to the right.

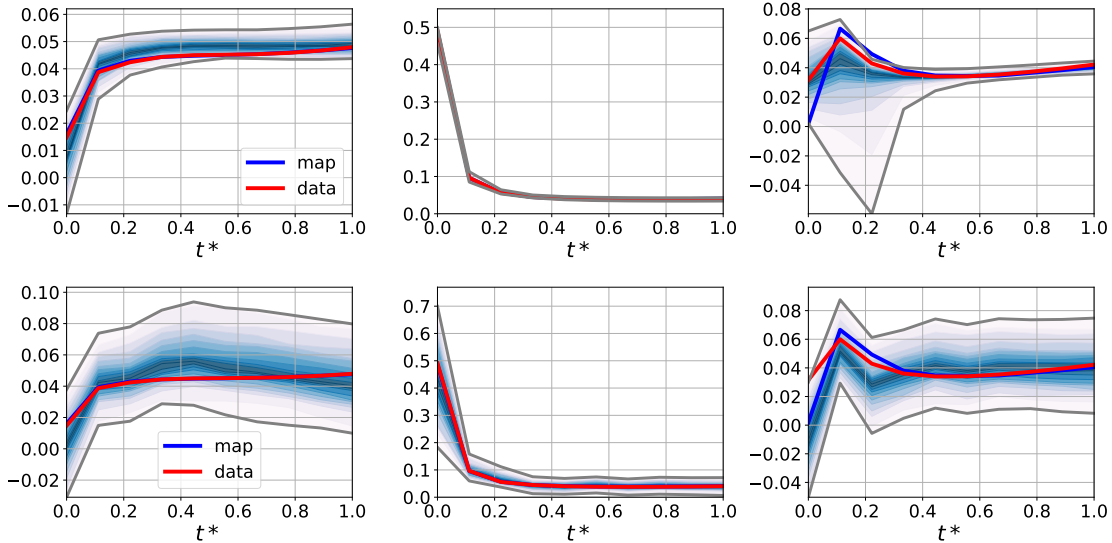


Figure 11: NODE: Three cases corresponding to minimum (left), median (middle), maximum (right) MAP discrepancy for training with $N_D = \frac{1}{2}N_w$ data points. Each plot show the MAP prediction, posterior push-forward distribution, and the corresponding data sample. Top row shows HMC results and bottom row shows SVGD results. Note the change in vertical scale from left panels to the right.

Finally, Fig. 13 and Fig. 14 show the average correlation of the predicted QoI at different time steps, defined as

$$c_{mn} = \langle [\Delta\hat{y}(X_i, f_i; w_{(j)})]_m [\Delta\hat{y}(X_i, f_i; w_{(j)})]_n \rangle \quad \text{with} \quad \Delta\hat{y}_i(X_i, f_i; w_{(j)}) \equiv \hat{y}_i(X_i, f_i; w_{(j)}) - \hat{y}_i(X_i, f_i; w_{\text{MAP}}) \quad (41)$$

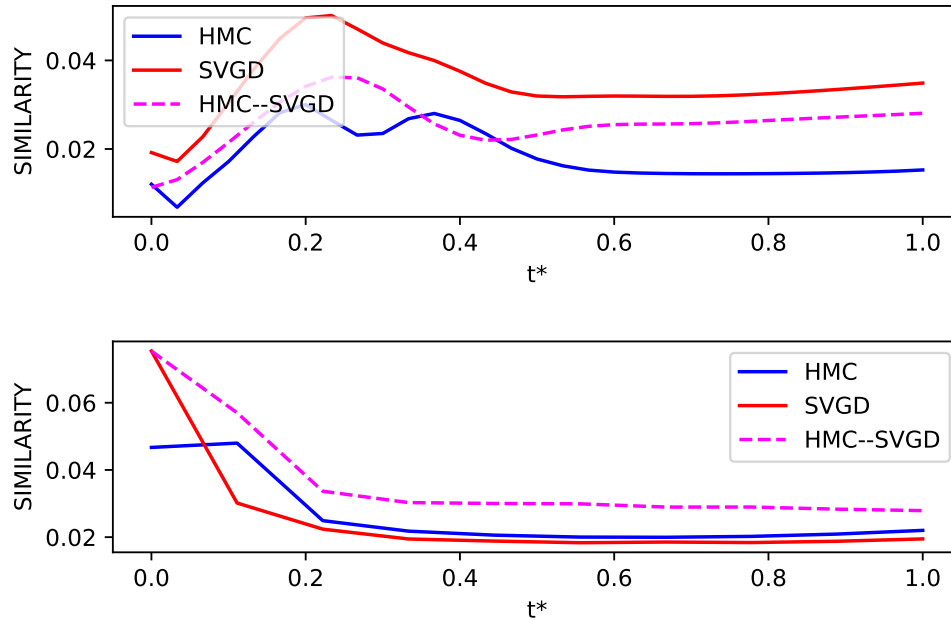


Figure 12: KSS similarity measures for (a) HMC versus observed data, (b) SVGD versus observed data, and (c) HMC versus SVGD; GRU (upper row) and NODE (lower row). A lower score indicates a greater similarity.

for two time steps t_m and t_n , and where the average (inner product) is over weight/model realizations (j) and input data samples i . The plots show that HMC and SVGD predict similar covariance structures albeit with some qualitative differences. For GRU, the HMC covariance structure is more diagonally dominant, while SVGD appears to be capturing significant cross correlation in the elastic-plastic transition. Likewise for the NODE, the HMC is diagonally dominant which SVGD appears to attribute more correlation of the initial conditions with all future states.

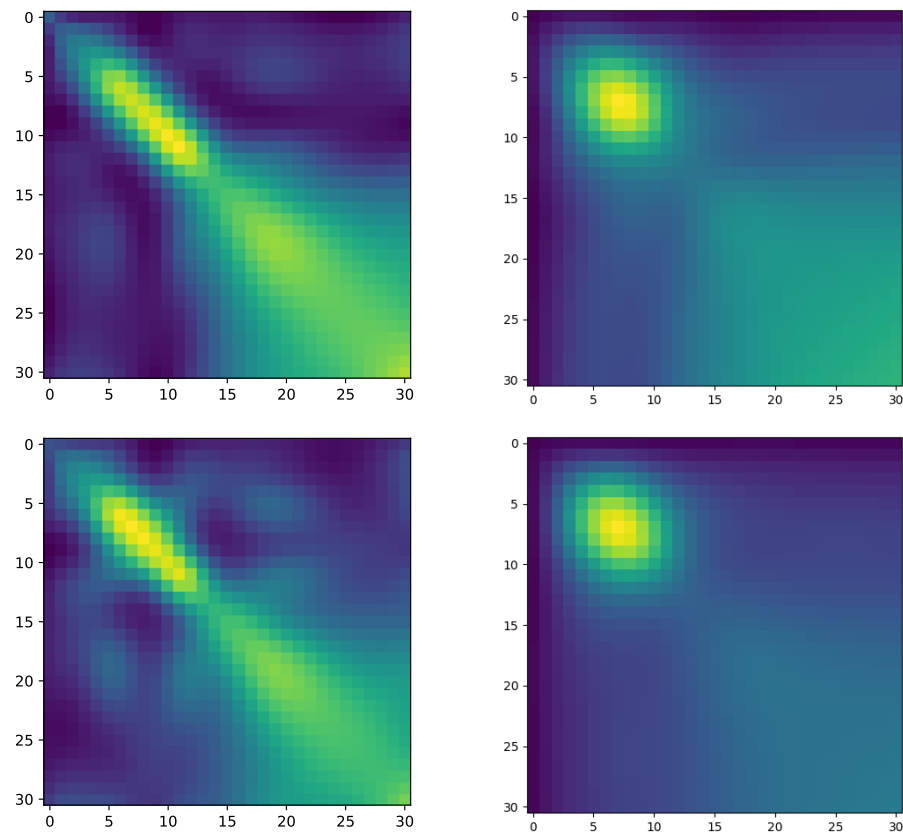


Figure 13: GRU: comparison of posterior push-forward correlations over time, comparing HMC (left) versus SVGD (right) for $N_D = \frac{1}{2}N_w$ (top) and $N_D = 2N_w$ (bottom). The x - and y -axis values are time-step n .

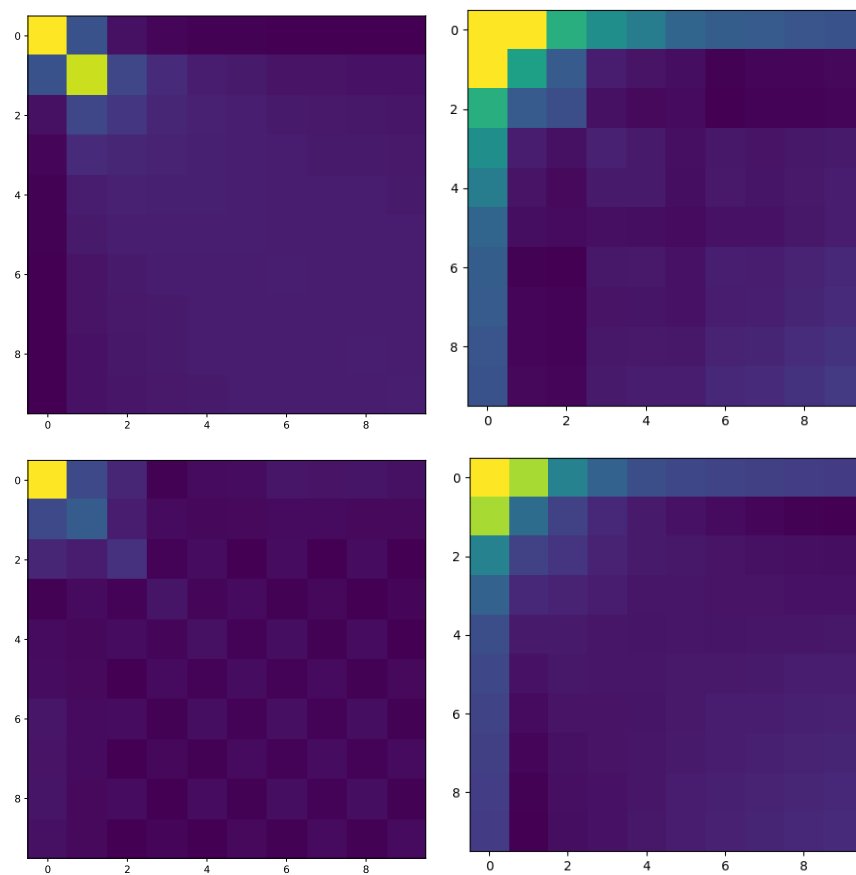


Figure 14: NODE: comparison of posterior push-forward correlations over time, comparing HMC (left) versus SVGD (right) for $N_D = \frac{1}{2}N_w$ (top) and $N_D = 2N_w$ (bottom). The x - and y -axis values are time-step n .

4.2 Comparison of SVGD and pSVG

In this section we demonstrate SVGD and pSVG on a model infeasible for HMC due to the high number of parameters. As mentioned in Sec. 3.1.2, we use a version of the GCNN-RNN crystal plasticity model operating on 3D data with 2609 parameters: 640 in convolution layers, 1680 in GRU, and rest in dense layers. Due to memory constraints, we can only propagate 32 particles per MAP in SVGD on a single GPU.

Fig. 15 shows the eigenspectrum of the Hessians of all the layers. Note the large range and the steep decay in magnitude. Fig. 15 also shows profile of reduction for two pSVG cases: 3% and 10% reduction in the active weight space. The parameters are primarily eliminated in the GRU which has the largest proportion of the weight and also controls the stability of the time evolution. Results at the high end of the eigenspectrum largely the same with $N_D = \{10, 100\}$ (not shown for brevity).

Fig. 16 shows the posterior push-forward for the three cases corresponding to minimum, median and maximum MAP discrepancy. In this figure we show the bundle of posterior push-forward trajectories to illustrate the quality of these distributions for SVGD, and pSVG with 3% and 10% reductions. The 3% reduction is visibly similar to the full SVGD; however, the realizations with 10% reduction indicate sampling of trajectories that appear to be marginally stable, which may be incurred from a relatively wide prior.

Fig. 17 compares the posterior push-forward correlations of the SVGD and pSVG with 3% reduction. The covariance structures are largely similar. The pSVG covariance structure shows more variance at the initial state and less in the elastic-plastic transition regime. In light of the benchmark illustration in Sec. 2.2 on the performance of pSVG on a problem with multiple connected maxima of the posterior, and the indications of a qualitatively similar scenario for this exemplar shown in Fig. 9, it is not surprising that pSVG gives a different PF covariance structure. At the same time, the pSVG covariance structure is much closer to the HMC results in the 2D case in Fig. 13, suggesting the ability of pSVG to achieve a more accurate posterior result due to its ability in achieving a higher particle-to-parameter ratio.

Fig. 18 shows the KSS similarity as defined earlier between the various posterior push-forward results compared to the data, and among results from the different algorithms. For $N_D = 1000$, SVGD and pSVG with 3% reduction are nearly indistinguishable except near initial state, while both are far from the 10% reduction. Fig. 18 shows the effect of dataset size. Clearly the posterior push-forward becomes farther from the data with less training data. At the same time the difference between full and projected SVGD becomes less, as the prior becomes more influential.

To explore whether the limitation on the number of simultaneous particles could be ameliorated by sampling from more MAPs, we ran an ensemble of 9 independent MAPs. Fig. 20 shows KSS similarity across results from multiple MAPs. It appears that the MAPs produce essentially equivalent results in terms of the posterior push-forward distributions.

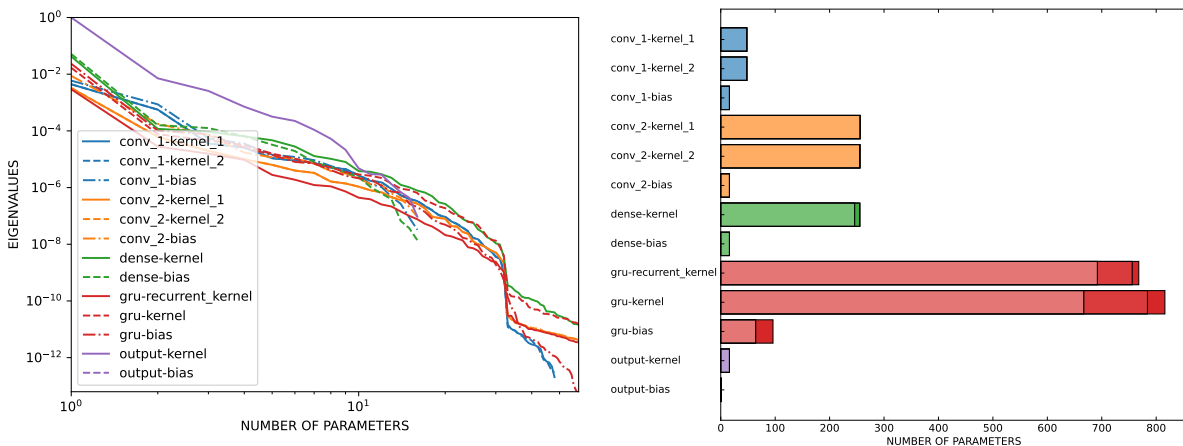


Figure 15: 3D GRU: eigenspectrums (left) and energy per layer and reduction profiles (right). For the reduction profiles, the three models—full, 17% reduction, and 32% reduction—are shown by stacked bars.

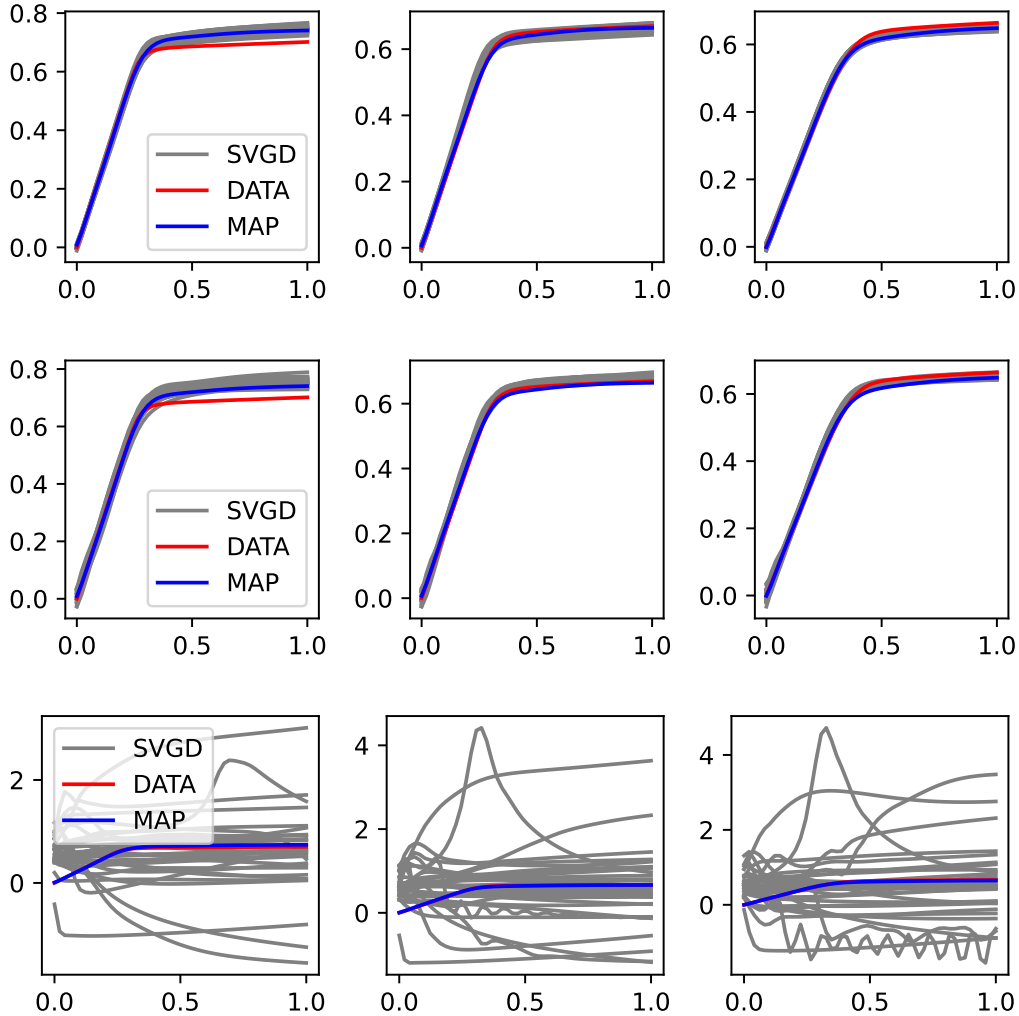


Figure 16: 3D GRU: posterior push-forward samples for three cases corresponding to minimum (left), median (center), and maximum (right) MAP discrepancy, for SVGD (top row) and pSVG with 3% (middle row) and 10% reductions (bottom row).

5 Conclusion

In this paper we employed two graph-based convolutional neural network (GCNN) architectures to model spatio-temporal process in two physical systems of practical interest. The first model employed a gated recurrent unit (GRU) to simulate the stress response in polycrystals, while the second model was based on a neural ordinary differential equation (NODE) to predict diffusion and gas release in an intergranular network. The discrepancy between the model and the data was framed in a Bayesian framework, which casts the neural network architecture to its Bayesian counterpart, and the resulting posterior parameter distribution was explored with both Hamiltonian Monte Carlo (HMC), Stein variational gradient descent (SVGD), and projected SVGD algorithms. We showed that SVGD produced posterior push-forward distributions that are similar to the reference results obtained via HMC, for both the GCNN-GRU and the GCNN-NODE models. Although the HMC chains were not well mixed due to the high-dimensionality of the models and the complexity of the posterior landscape and the SGVD particle ensembles were at best on par with the size of the parameter space, the posterior push-forward distribution profiles through time were similar with each other and consistent with observed data. HMC results illustrated the convoluted seemingly low dimensional manifold of the likely model weights. We attribute this to both the slow mixing of the chains as well as to the highly irregular posterior landscape to be expected for NN models.

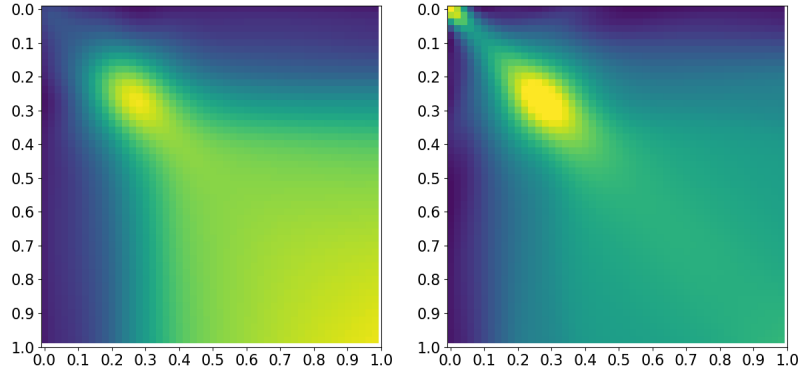


Figure 17: 3D GRU: comparison of posterior push-forward correlations over time, for SVGD (left) and pSVGD with 3% reduction (right).

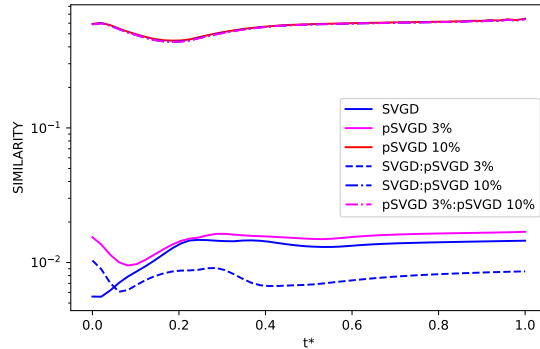


Figure 18: 3D GRU: KSS similarity measures between SVGD and data, and pSVGD and data (solid lines); and among these algorithms (dashed). A lower similarity score indicates a greater similarity.

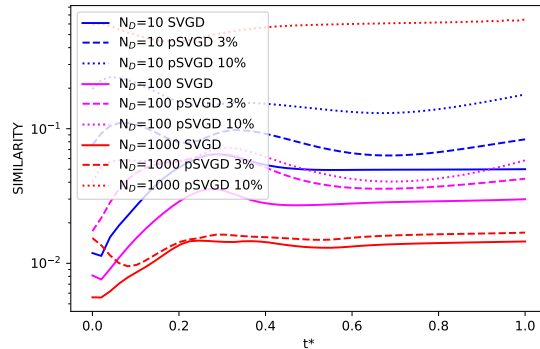


Figure 19: 3D GRU: KSS similarity measures between SVGD (solid), 3% reduction pSVGD (dashed) and 10% reduction pSVGD (dotted) versus data for $N_D = \{10, 100, 1000\}$ (blue, magenta, red). A lower similarity score indicates a greater similarity.

Our particle ensembles were limited by memory on a single GPU, which could be expanded by distributing the ensemble across multiple GPUs as suggested by Chen and Ghattas [73]. Being limited to less particles than dimensions, we may not have sampled the full covariance structure but the results did appear to produce posterior push-forward distributions that are consistent with the observed data. The projection from pSVGD proved less effective than we hoped, in part due to impairing the stability of the time-evolution in the recurrent neural network model by pruning its weight space, but also due to the convoluted posterior manifold. As illustrated in Sec.2.2, the convoluted submanifold

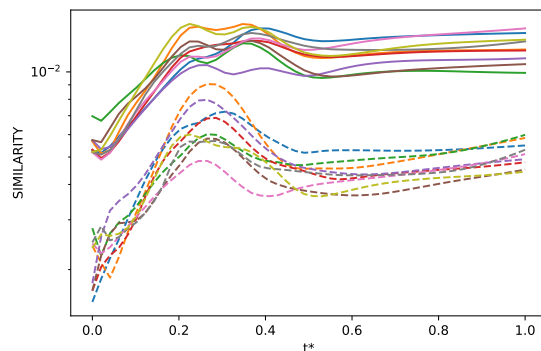


Figure 20: 3D GRU: KSS similarity measures for SVGD versus data based on an ensemble of different MAPs (solid) and between each SVGD result with the rest of the ensemble (dashed).

likely does not yield to accurate reduction as a subspace. Updating the projection as the particles move through the posterior landscape may help but the coordination of the particles constrains the pSVG method to a single subspace for all particles, and is essentially a Laplace-like approximation.

In future work we will explore nonlinear model reduction techniques to further improve SVGD for these type of problems.

Acknowledgements

Tensorflow [74] and Spektral [75] were used to implement the models and methods of this work. This open-source software is gratefully acknowledged. CS and REJ would like to thank Prof. M. Tonks (Univ. Florida) and his group for the inspiration for the gas release exemplar. XH and JH acknowledge funding support by the U.S. Department of Energy, Office of Science, Office of Advanced Scientific Computing Research, under Award Number DE-SC0021397. This material is based upon work supported by the U.S. Department of Energy, Office of Science, Advanced Scientific Computing Research program. Sandia National Laboratories is a multimission laboratory managed and operated by National Technology and Engineering Solutions of Sandia, LLC., a wholly owned subsidiary of Honeywell International, Inc., for the U.S. Department of Energy's National Nuclear Security Administration under contract DE-NA-0003525. This paper describes objective technical results and analysis. Any subjective views or opinions that might be expressed in the paper do not necessarily represent the views of the U.S. Department of Energy or the United States Government.

References

- [1] Nathan Baker, Frank Alexander, Timo Bremer, Aric Hagberg, Yannis Kevrekidis, Habib Najm, Manish Parashar, Abani Patra, James Sethian, Stefan Wild, and Karen Willcox. Workshop Report on Basic Research Needs for Scientific Machine Learning: Core Technologies for Artificial Intelligence. Technical report, U.S. Department of Energy Office of Science (SC), 2019.
- [2] Ari L Frankel, Reese E Jones, Coleman Alleman, and Jeremy A Templeton. Predicting the mechanical response of oligocrystals with deep learning. *Computational Materials Science*, 169:109099, 2019.
- [3] Ari Frankel, Kousuke Tachida, and Reese Jones. Prediction of the evolution of the stress field of polycrystals undergoing elastic-plastic deformation with a hybrid neural network model. *Machine Learning: Science and Technology*, 2020.
- [4] Ari L Frankel, Cosmin Safta, Coleman Alleman, and Reese Jones. Mesh-based graph convolutional neural networks for modeling materials with microstructure. *Journal of Machine Learning for Modeling and Computing*, 3(1), 2022.
- [5] Reese Jones, Cosmin Safta, and Ari Frankel. Deep learning and multi-level featurization of graph representations of microstructural data. *Computational Mechanics*, 72(1):57–75, 2023.
- [6] Maziar Raissi. Deep hidden physics models: Deep learning of nonlinear partial differential equations. *The Journal of Machine Learning Research*, 19(1):932–955, 2018.

- [7] Maziar Raissi, Paris Perdikaris, and George E Karniadakis. Physics-informed neural networks: A deep learning framework for solving forward and inverse problems involving nonlinear partial differential equations. *Journal of Computational physics*, 378:686–707, 2019.
- [8] Lu Lu, Pengzhan Jin, and George Em Karniadakis. Deeponet: Learning nonlinear operators for identifying differential equations based on the universal approximation theorem of operators. *arXiv preprint arXiv:1910.03193*, 2019.
- [9] Chayan Banerjee, Kien Nguyen, Clinton Fookes, and Maziar Raissi. A survey on physics informed reinforcement learning: Review and open problems. *arXiv preprint arXiv:2309.01909*, 2023.
- [10] Ruben Villarreal, Nikolaos N Vlassis, Nhon N Phan, Tommie A Catanach, Reese E Jones, Nathaniel A Trask, Charlotte LB Kramer, and WaiChing Sun. Design of experiments for the calibration of history-dependent models via deep reinforcement learning and an enhanced kalman filter. *Computational Mechanics*, 72(1):95–124, 2023.
- [11] Wanggang Shen and Xun Huan. Bayesian sequential optimal experimental design for nonlinear models using policy gradient reinforcement learning. *Computer Methods in Applied Mechanics and Engineering*, 416:116304, 2023.
- [12] Simon S Du, Xiyu Zhai, Barnabas Poczos, and Aarti Singh. Gradient descent provably optimizes over-parameterized neural networks. *arXiv preprint arXiv:1810.02054*, 2018.
- [13] Mahdi Soltanolkotabi, Adel Javanmard, and Jason D Lee. Theoretical insights into the optimization landscape of over-parameterized shallow neural networks. *IEEE Transactions on Information Theory*, 65(2):742–769, 2018.
- [14] Difan Zou and Quanquan Gu. An improved analysis of training over-parameterized deep neural networks. *Advances in neural information processing systems*, 32, 2019.
- [15] James O. Berger. *Statistical Decision Theory and Bayesian Analysis*. Springer Series in Statistics. Springer New York, New York, NY, 1985.
- [16] D. S. Sivia and J. Skilling. *Data Analysis: A Bayesian Tutorial*. Oxford University Press, New York, NY, 2nd edition, 2006.
- [17] Udo Von Toussaint. Bayesian inference in physics. *Reviews of Modern Physics*, 83:943–999, 2011.
- [18] David J. C. MacKay. A Practical Bayesian Framework for Backpropagation Networks. *Neural Computation*, 4(3):448–472, 1992.
- [19] Radford M. Neal. *Bayesian Learning for Neural Networks*. Springer-Verlag New York, New York, NY, 1996.
- [20] Alex Graves. Practical Variational Inference for Neural Networks. In *Advances in Neural Information Processing Systems 24 (NIPS 2011)*, pages 2348–2356, Granada, Spain, 2011.
- [21] Charles Blundell, Julien Cornebise, Koray Kavukcuoglu, and Daan Wierstra. Weight Uncertainty in Neural Networks. In *Proceedings of the 32nd International Conference on Machine Learning*, volume 37, pages 1613–1622, 2015.
- [22] Yarin Gal. *Uncertainty in Deep Learning*. PhD thesis, University of Cambridge, 2016.
- [23] Christophe Andrieu, Nando de Freitas, Arnaud Doucet, and Michael I. Jordan. An Introduction to MCMC for Machine Learning. *Machine Learning*, 50:5–43, 2003.
- [24] Steve Brooks, Andrew Gelman, Galin Jones, and Xiao-Li Meng, editors. *Handbook of Markov Chain Monte Carlo*. Chapman-Hall/CRC, 2011.
- [25] Simon Duane, A.D. Kennedy, Brian J. Pendleton, and Duncan Roweth. Hybrid Monte Carlo. *Physics Letters B*, 195(2):216–222, sep 1987.
- [26] Qi He and Jack Xin. Hybrid deterministic-stochastic gradient Langevin dynamics for Bayesian learning. *Communications in Information and Systems*, 12(3):221–232, 2012.
- [27] Tianqi Chen, Emily B. Fox, and Carlos Guestrin. Stochastic Gradient Hamiltonian Monte Carlo. In *Proceedings of the 31st International Conference on Machine Learning*, volume 32, pages 1683–1691, Beij, 2014.
- [28] Cheng Zhang, Babak Shahbaba, and Hongkai Zhao. Variational Hamiltonian Monte Carlo via Score Matching. *Bayesian Analysis*, 13(2):485–506, jun 2018.
- [29] David M. Blei, Alp Kucukelbir, and Jon D. McAuliffe. Variational Inference: A Review for Statisticians. *Journal of the American Statistical Association*, 112(518):859–877, 2017.
- [30] Cheng Zhang, Judith Butepage, Hedvig Kjellstrom, and Stephan Mandt. Advances in Variational Inference. *IEEE Transactions on Pattern Analysis and Machine Intelligence*, 41(8):2008–2026, 2019.

- [31] Qiang Liu and Dilin Wang. Stein Variational Gradient Descent: A General Purpose Bayesian Inference Algorithm. In *Advances in Neural Information Processing Systems 29 (NIPS 2016)*, pages 2378–2386, Barcelona, Spain, 2016.
- [32] Jingwei Zhuo, Chang Liu, Jiaxin Shi, Jun Zhu, Ning Chen, and Bo Zhang. Message passing Stein variational gradient descent. In *35th International Conference on Machine Learning, ICML 2018*, volume 13, pages 9629–9638, 2018.
- [33] Dilin Wang, Zhe Zeng, and Qiang Liu. Stein variational message passing for continuous graphical models. In *35th International Conference on Machine Learning, ICML 2018*, volume 12, pages 8278–8289, 2018.
- [34] Peng Chen and Omar Ghattas. Projected stein variational gradient descent. In *Advances in Neural Information Processing Systems*, 2020.
- [35] Myles Morelli, Jeremiah Hauth, Alberto Guardone, Xun Huan, and Beckett Y. Zhou. A rotorcraft in-flight ice detection framework using computational aeroacoustics and Bayesian neural networks. *Structural and Multidisciplinary Optimization*, 66:197, 2023.
- [36] Jeremiah Hauth. *Advances in Intuitive Priors and Scalable Algorithms for Bayesian Deep Neural Network Models in Scientific Applications*. PhD thesis, University of Michigan, 2024.
- [37] Larry K Aagesen, David Andersson, Benjamin W Beeler, Michael WD Cooper, Kyle A Gamble, Yinbin Miao, Giovanni Pastore, and Michael R Tonks. Phase-field simulations of intergranular fission gas bubble behavior in U3Si2 nuclear fuel. *Journal of Nuclear Materials*, 541:152415, 2020.
- [38] Dong-Uk Kim, Sophie Blondel, David E Bernholdt, Philip Roth, Fande Kong, David Andersson, Michael R Tonks, and Brian D Wirth. Modeling mesoscale fission gas behavior in uo2 by directly coupling the phase field method to spatially resolved cluster dynamics. *Materials Theory*, 6(1):7, 2022.
- [39] Xingjian Shi, Zhourong Chen, Hao Wang, Dit-Yan Yeung, Wai-Kin Wong, and Wang-chun Woo. Convolutional lstm network: A machine learning approach for precipitation nowcasting. *Advances in neural information processing systems*, 28, 2015.
- [40] Reza Azad, Maryam Asadi-Aghbolaghi, Mahmood Fathy, and Sergio Escalera. Bi-directional convlstm u-net with densely connected convolutions. In *Proceedings of the IEEE/CVF international conference on computer vision workshops*, pages 0–0, 2019.
- [41] Zhihui Lin, Maomao Li, Zhuobin Zheng, Yangyang Cheng, and Chun Yuan. Self-attention convlstm for spatiotemporal prediction. In *Proceedings of the AAAI conference on artificial intelligence*, volume 34:07, pages 11531–11538, 2020.
- [42] Sepp Hochreiter and Jürgen Schmidhuber. Long short-term memory. *Neural computation*, 9(8):1735–1780, 1997.
- [43] Kyunghyun Cho, Bart Van Merriënboer, Caglar Gulcehre, Dzmitry Bahdanau, Fethi Bougares, Holger Schwenk, and Yoshua Bengio. Learning phrase representations using rnn encoder-decoder for statistical machine translation. *arXiv preprint arXiv:1406.1078*, 2014.
- [44] Tian Qi Chen, Yulia Rubanova, Jesse Bettencourt, and David K Duvenaud. Neural ordinary differential equations. In *Advances in neural information processing systems*, pages 6571–6583, 2018.
- [45] Emilien Dupont, Arnaud Doucet, and Yee Whye Teh. Augmented neural odes. *Advances in neural information processing systems*, 32, 2019.
- [46] Ernst Hairer, Syvert P Nørsett, and Gerhard Wanner. Solving ordinary differential equations i: Non-stiff problems, volume 8 of *springer series in comput. mathematics*, 1993.
- [47] Gerhard Wanner and Ernst Hairer. *Solving ordinary differential equations II: Stiff and Differential-Algebraic Problems*, volume 375. Springer Berlin Heidelberg New York, 1996.
- [48] Ernst Hairer, Christian Lubich, and Gerhard Wanner. *Geometric Numerical Integration: Structure-Preserving Algorithms for Ordinary Differential Equations*, volume 31. Springer Science & Business Media, 2006.
- [49] Michael Betancourt. A conceptual introduction to Hamiltonian Monte Carlo. *arXiv preprint arXiv:1701.02434*, 2017.
- [50] Dilin Wang, Ziyang Tang, Chandrajit Bajaj, and Qiang Liu. Stein variational gradient descent with matrix-valued kernels. *Advances in neural information processing systems*, 32, 2019.
- [51] Nathan Halko, Per-Gunnar Martinsson, and Joel A Tropp. Finding structure with randomness: Probabilistic algorithms for constructing approximate matrix decompositions. *SIAM review*, 53(2):217–288, 2011.

- [52] Ronald R. Coifman and Stéphane Lafon. Diffusion maps. *Applied and Computational Harmonic Analysis*, 21(1):5–30, 2006.
- [53] C. Soize and R. Ghanem. Data-driven probability concentration and sampling on manifold. *Journal of Computational Physics*, 321:242–258, 2016.
- [54] David Montes de Oca Zapiain and Surya R Kalidindi. Localization models for the plastic response of polycrystalline materials using the material knowledge systems framework. *Modelling and Simulation in Materials Science and Engineering*, 27(7):074008, 2019.
- [55] Ari Frankel, Kousuke Tachida, and Reese Jones. Prediction of the evolution of the stress field of polycrystals undergoing elastic-plastic deformation with a hybrid neural network model. *Machine Learning: Science and Technology*, 1(3):035005, 2020.
- [56] Nikolaos N Vlassis and WaiChing Sun. Sobolev training of thermodynamic-informed neural networks for interpretable elasto-plasticity models with level set hardening. *Computer Methods in Applied Mechanics and Engineering*, 377:113695, 2021.
- [57] David Montes de Oca Zapiain, Hojun Lim, Taejoon Park, and Farhang Pourboghraat. Predicting plastic anisotropy using crystal plasticity and bayesian neural network surrogate models. *Materials Science and Engineering: A*, 833:142472, 2022.
- [58] Nikolaos N Vlassis and WaiChing Sun. Geometric learning for computational mechanics part ii: Graph embedding for interpretable multiscale plasticity. *Computer Methods in Applied Mechanics and Engineering*, 404:115768, 2023.
- [59] Paul R Dawson. Computational crystal plasticity. *International journal of solids and structures*, 37(1-2):115–130, 2000.
- [60] Franz Roters, Philip Eisenlohr, Luc Hantcherli, Denny Dharmawan Tjahjanto, Thomas R Bieler, and Dierk Raabe. Overview of constitutive laws, kinematics, homogenization and multiscale methods in crystal plasticity finite-element modeling: Theory, experiments, applications. *Acta Materialia*, 58(4):1152–1211, 2010.
- [61] UF Kocks. Laws for work-hardening and low-temperature creep. *Journal of engineering materials and technology*, 98(1):76–85, 1976.
- [62] H Mecking, UF Kocks, and H Fischer. Hardening, recovery, and creep in fcc mono-and polycrystals. In *Presented at the 4th Intern. Conf. on Strength of Metals and Alloys, Nancy, 30 Aug.-3 Sep. 1976*, 1976.
- [63] Thomas N Kipf and Max Welling. Semi-supervised classification with graph convolutional networks. *arXiv preprint arXiv:1609.02907*, 2016.
- [64] Gilbert Strang. On the construction and comparison of difference schemes. *SIAM journal on numerical analysis*, 5(3):506–517, 1968.
- [65] Alexandre Joel Chorin. Numerical solution of the Navier-Stokes equations. *Mathematics of computation*, 22(104):745–762, 1968.
- [66] Glenn J Martyna, Mark E Tuckerman, Douglas J Tobias, and Michael L Klein. Explicit reversible integrators for extended systems dynamics. *Molecular Physics*, 87(5):1117–1157, 1996.
- [67] Diederik P Kingma and Jimmy Ba. Adam: A method for stochastic optimization. *arXiv preprint arXiv:1412.6980*, 2014.
- [68] Khue-Dung Dang, Matias Quiroz, Robert Kohn, Tran Minh-Ngoc, and Mattias Villani. Hamiltonian Monte Carlo with energy conserving subsampling. *Journal of machine learning research*, 20, 2019.
- [69] Laurens van der Maaten and Geoffrey Hinton. Visualizing data using t-sne. *Journal of Machine Learning Research*, 9(86):2579–2605, 2008.
- [70] Mikhail Belkin and Partha Niyogi. Laplacian eigenmaps for dimensionality reduction and data representation. *Neural Computation*, 15(6):1373–1396, 2003.
- [71] Gábor J Székely, Maria L Rizzo, and Nail K Bakirov. Measuring and testing dependence by correlation of distances. *The Annals of Statistics*, 35(6):2769, 2007.
- [72] Gábor J Székely and Maria L Rizzo. Brownian distance covariance. *The annals of applied statistics*, pages 1236–1265, 2009.
- [73] Peng Chen and Omar Ghattas. Projected Stein variational gradient descent. *Advances in Neural Information Processing Systems*, 33:1947–1958, 2020.

- [74] Martín Abadi, Ashish Agarwal, Paul Barham, Eugene Brevdo, Zhifeng Chen, Craig Citro, Greg S. Corrado, Andy Davis, Jeffrey Dean, Matthieu Devin, Sanjay Ghemawat, Ian Goodfellow, Andrew Harp, Geoffrey Irving, Michael Isard, Yangqing Jia, Rafal Jozefowicz, Lukasz Kaiser, Manjunath Kudlur, Josh Levenberg, Dandelion Mané, Rajat Monga, Sherry Moore, Derek Murray, Chris Olah, Mike Schuster, Jonathon Shlens, Benoit Steiner, Ilya Sutskever, Kunal Talwar, Paul Tucker, Vincent Vanhoucke, Vijay Vasudevan, Fernanda Viégas, Oriol Vinyals, Pete Warden, Martin Wattenberg, Martin Wicke, Yuan Yu, and Xiaoqiang Zheng. TensorFlow: Large-scale machine learning on heterogeneous systems, 2015. Software available from tensorflow.org.
- [75] Daniele Grattarola and Cesare Alippi. Graph neural networks in tensorflow and keras with spektral [application notes]. *IEEE Computational Intelligence Magazine*, 16(1):99–106, 2021.